Observation of Topological Berry phase in a plasmonic system

A Thesis Submitted to the University of Manchester for the Degree of

Master of Philosophy

In the Faculty of Faculty of Science & Engineering

2021

Kaiyuan Wang

School of Natural Science

Department of Material

Supervisor: Prof. Coskun Kocabas

Content

DECLARATION *4*

COPYRIGHT STATEMENT *5*

List of figures *6*

List of tables *8*

List of abbreviation *8*

Abstract *10*

Chapter 1 Introduction *12*

Chapter 2 One dimensional wave dynamics *13*

2.1 The concept of impedance *13*

2.2 Transmission of electromagnetic waves *18*

Chapter 3 Topology and Photonics *25*

3.1 The concept of topology *25*

3.2 Progress in topological photonics *27*

3.2.1 One dimensional topological photonic system *29*

3.2.2 Two dimensional topological photonic system *32*

3.2.2.1 Photonic Integer Quantum Hall Effect in two dimensional topological optical systems *32*

3.2.2.2 Photonic Quantum Spin Hall Effect in two dimensional topological optical systems *33*

3.2.3 Floquet topological insulator *37*

3.2.4 New topological effects in photonics *38*

3.2.4.1 Non-hermitian topological photonic effects *38*

3.2.4.2 Nonlinear topological photonic effects *39*

3.2.4.3 Higher order topological photonic effects *41*

Chapter 4 Topology and geometrical phase *45*

4.1 Topology in Surface plasmon polaritons *45*

4.2 Geometric phase *46*

Chapter 5 Experimental setup and materials： *52*

5.1 Materials and optical components used in the experiments *52*

5.2 Excitation of surface plasmon polaritons *54*

5.3 Experimental setup used for measurement of reflection phase *60*

5.4 Working principle of the Wollaston prism: *62*

5.5 Interferogram of broad-band light source: *63*

5.6 Fourier transform of the interferogram: *65*

5.7 Imaging camera: *68*

5.8 Data acquisition and analysis software: *69*

5.9 Sample preparation method: *73*

Chapter 6 Results and discussion: 75

Chapter 7 Conclusion 86

Reference: *87*

DECLARATION

No portion of the work referred to in the thesis has been submitted in support of an application for another degree or qualification of this or any other university or other institute of learning.

Kaiyuan Wang

COPYRIGHT STATEMENT

List of figures

Figure 1 The transmission line model consisting of series of capacitors and inductors.

Figure 2 Representation of voltage wave on a transmission line.

Figure 3 The Smith chart.

The colour map represents the phase of reflectivity as a function of complex impedance Z.

Figure 5 The concept of topology uses integer numbers to clarify geometrical objects.

Figure 6 shows two closed loops C1 and C2 which are topologically different.

Figure 7 Schematic diagram of SSH model, each cell contains two lattice points

Figure 8 Topological photonics in 1D SSH model.

Figure 9 Schematic of the waveguide composed of an interface between a gyromagnetic photonic crystal slab and a metal wall.

Figure 10 Photonic Quantum Spin Hall Effect with polarization degree of freedom

Figure 11 A Photonic crystal with hexagonal lattice used to demonstrate a topologically trivial and nontrivial crystal by deforming the position of the pillars in the radial directions.

Figure 12 Coupled ring resonators which acquire different phase depending on the coupling direction.

Figure 13 Topological photonics using coupled waveguide arrays.

Figure 14 Non-hermitian light regulation in topological microring lattices.

Figure 15 Nonlinearity-induced photonic topological insulator and its regime.

Figure 16 A quad-coupler and the measured angular photon distribution probability.

Figure 17 Two different configurations were used to excite surface plasmon polaritons.

Figure 18 Transporting a vector on parameter space.

Figure 19 Experimental setup showing the excitation of surface plasmon polaritons with Kretschmann configuration.

Figure 20 The variation of the reflected intensity as a function of incidence angle for different metal thicknesses.

Figure 21 Dispersion curve of light and SPPs.

Figure 22 Image of the reflected light from the sample with two different metal thicknesses.

Figure 23 Schematics and photographs of the experimental setup used for the measurement of the reflection phase.

Figure 24 Schematic drawing of the Wollaston prism and the angular deviation as a function of wavelengths.

Figure 25 Schematic showing the optical path for the interferogram.

Figure 26 The recorded image and the graph shows the interferogram of the reflected light from the prism.

Figure 27 Spectral and phase changes of the beam obtained by Fourier transform visible interferogram.

Figure 28 The LabView program logic block diagram of the interferometer to perform data acquisition and analysis.

Figure 29 Block diagram of the Labview results of the interferometer.

Figure 30 Desktop sputtering system used for the deposition of the metal for the surface plasmons.

Figure 31 Schematic representation of the Kretschmann configuration used for the observation of the Berry phase and winding number plus domain colour.

Figure 32 Experimental results showing the reflection phase and amplitude for different metal thickness for a spectral range from 450 to 800 nm.

Figure 33 Experimentally obtained phase map of reflection plotted against thickness and wavelength.

Figure 34 Schematic showing the excitation of SPPs on topologically different surfaces using a monochromatic light source which generates a uniform interference pattern.

Figure 35 Images show the reflection image from a surface with 4 different metal thicknesses and a special character.

List of tables

Table 1 Materials and equipment using in this project.

List of abbreviation

SPPs	Surface plasmon polaritons
2D	Two-dimensional
3D	Three-dimensional
Cs	Chern number
TKNN	Thouless-Kohmoto-Nijs
SSH	Su-Schrieffer–Heeger
TM	Transverse Magnetic
TE	Transverse Electric
PhC	Photonic crystal
CW	Clockwise
CCW	Counter clockwise
A*R*	Augmented reality
SCL	Supercontinuum laser

WP	Wollaston prism
CMOS	Complementary metal–oxide–semiconductor
CCD	Charge-coupled device
ZPD	Zero-phase-difference
PD	Path difference
AC	Alternating current
DC	Direct current

Abstract

Topological photonics has attracted great interest in the past few years because it reveals exciting fundamental advances in the way we can control light with engineered materials and the vast opportunities for applications. This area of research draws inspiration from recent advances in condensed matter physics, highlighting the important connection between the topological features of the energy band diagram of infinite periodic media and the electronic response of finite samples. In particular, topological insulators are a class of insulating materials with non-trivial topological characteristics of their bandgap, based on which robust conduction properties are expected at the boundary of any finite sample of such materials. Their inherent robustness is rooted in these topological features and is unaffected by continuous perturbations and local disorder. These electronic properties are protected by the underlying symmetry protection that drives the nontrivial topology. The extraordinary robustness of the features has led to compelling new nano-optical devices such as reconfigurable waveguides, disorder-resistant irreversible transport, quantum optics, and intense lasers.

In this thesis, we discovered the existence of a topological phenomenon in a plasmonic system. We observed the Berry phase for surface plasmon polaritons on a flat metallic surface. The observed Berry phase is determined by the thickness of the metal layer which changes the interplay between the directly reflected light and light that out-coupled from the excited plasma. The interference of these out of phase components provides a topological character that can be observed in the complex optical reflectivity coefficient. We found that topological character can lead to stable boundary states which generate complete absorption of light at the boundary between topologically different domains. Our observations of the topological property of surface plasmon polaritons would lead to a new type of plasma-based nanophotonic device. In addition, these results also inspire the discovery of Berry phases and topological properties in

other optical systems such as optical resonators.

Chapter 1 Introduction

Surface plasmon polaritons (SPPs) are localised surface waves that enable nanoscale light manipulation and the development of nanoscale photonic circuits. Owing to their inherent loss, they provide an ideal platform to study non-Hermitian topology by engineering the plasmonic band structure. Here, we provide a new topological perspective in the excitations of SPPs on a flat surface. We show that the balance between the internal loss and the excitation defines the topology of the reflection. We experimentally observed a topologically-protected 2π Berry phase by encircling a singularity in the reflectivity. We anticipate that these results provide realistic pathways for utilising topological properties in photonic circuits even on the visible spectrum.

The thesis is structured as follow:

Chapter 1 provides an overview of the thesis and the general idea.

In Chapter 2, I will discuss the concept of wave impedance which provides a simple way of understanding electromagnetic waves and their reflectivity from interfaces. I will provide the basic formalism and derivation of wave impedance using circuit elements then generalize the impedance concept for electromagnetic waves. This formalism helps calculation of complex optical reflectivity and the phase singularity in the reflection.

In chapter 3, I will talk about the concept of topology in optics. I will give a couple of examples from the literature that use different optical systems to demonstrate the topological character of light.

Chapter 4 covers the topology of surface plasmon polaritons. I will discuss the basic experimental configuration.

In Chapter 5, I will provide details of the materials and methods used in this thesis. We have built an interferometric spectrometer to measure the intensity and phase of the reflected light. the Berry phase from the recorded interference pattern.

In Chapter 6, I will discuss the results and topological interpretation of these results.

Chapter 7 will provide the concussion and future direction for this research.

Chapter 2 One dimensional wave dynamics

2.1 The concept of impedance

Since "impedance" is first introduced by Oliver Heaviside in 1886, it plays an important role in circuit analysis. Impedance is a general term for the resistance, inductance, and capacitance in the circuit that hinder the alternating current. Impedance is a complex number, the real part is called resistance, and the imaginary part is called reactance. Impedance extends the concept of resistance to the field of AC circuits, not only describing the relative amplitude of voltage and current but also describing their relative phase. When there is direct current running in the circuit, the resistance is equal to the impedance, and the resistance can be regarded as an impedance with zero phase.

The concept of impedance can also be extended to the propagation of waves. The wave impedance of an electromagnetic wave is the ratio of the transverse component of the electric field and the magnetic field. That is:

$$Z = \frac{\vec{E}}{\vec{H}} \tag{2.1.1}$$

To accurately express impedance, we need to introduce the concept of the transmission line. The transmission line model can describe plane waves well, and plane waves are often used to represent radiation fields at radio, microwave, and optical frequencies.

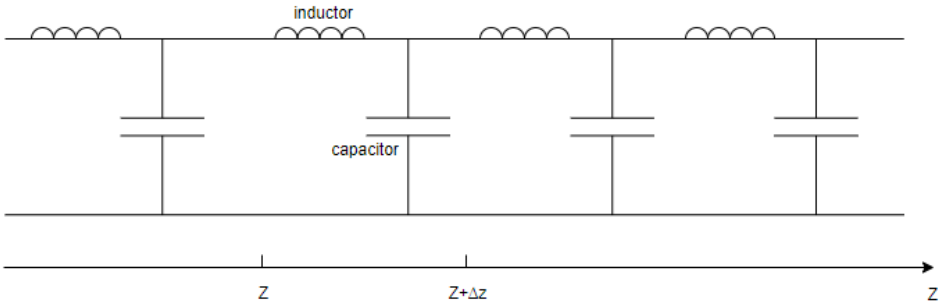

Figure 1 The transmission line model consisting of series of capacitors and inductors. This model can be generalised to understand the broad range of wave systems including electromagnetic waves and plasmons.

As shown in Figure 1, on any finite axial length, there is an infinite set of basic units, as shown in the figure, there are series capacitors and inductances. The parameters L and C are defined in terms of unit length. Therefore, for the section between $z + \Delta z$ and z, $L\Delta z$ is the series inductance of a section when the distributed line has a length of Δz (expressed in Henry's formula), and $C\Delta z$ is the parallel capacitance (in Farads). At the limit of the incremental length $\Delta z \rightarrow 0$, the distribution parameter to the transmission line can be used as a model for three kinds of electromagnetic field propagation:

- First, an accurate representation of uniformly polarized electromagnetic waves and plane waves is given
- Secondly, the distributed parameter transmission line accurately represents the coordinate and time dependence of the transient electromagnetic wave propagating on the axially uniform perfect guide forming an arbitrary cross-section transmission line.
- Thirdly, it approximates the dependence of coordinate and time on the system with a large aspect ratio.

According to Kirchhoff's law, the currents into the node of the elemental section sum to zero:

$$I(z) - I(z + \Delta z) = C\Delta z \frac{\partial V}{\partial t} \tag{2.1.2}$$

Similarly:

$$V(z) - V(z + \Delta z) = L\Delta z \frac{\partial I}{\partial t} \tag{2.1.3}$$

According to the definition of derivative:

$$\lim_{\Delta Z \to 0} \frac{f(z + \Delta z) - f(z)}{\Delta z} = \frac{\partial f}{\partial z} \tag{2.1.4}$$

Combining equation (2.1.2) with (2.1.3) (2.1.4) respectively, we can get:

$$\frac{\partial I}{\partial z} = -C \frac{\partial V}{\partial t} \tag{2.1.5}$$

$$\frac{\partial V}{\partial z} = -L \frac{\partial I}{\partial t} \tag{2.1.6}$$

The evolution of the transmission line voltage $V(z,t)$ and its related transient electromagnetic field is controlled by the one-dimensional wave equation. Combining the transmission line equations (2.1.2)-(2.1.6), an expression for *V* is obtained.

$$\frac{\partial^2 I}{\partial z \partial t} = -C \frac{\partial^2 V}{\partial t^2}$$

$$\frac{\partial^2 V}{\partial z^2} = -L \frac{\partial^2 I}{\partial z \partial t}$$

$$\frac{\partial^2 V}{\partial z^2} = CL \frac{\partial^2 V}{\partial t^2} = \frac{1}{c^2} \frac{\partial^2 V}{\partial t^2} \tag{2.1.7}$$

This equation has a remarkably general pair of solutions:

$$V = V_+(\alpha) + V_-(\beta) \tag{2.1.8}$$

Where V_+ and V_- are arbitrary functions of the variables *α* and *β*, and they are defined as special combinations of the independent variables *z* and *t*.

$$\alpha = z - xt \qquad\qquad \beta = z + xt \tag{2.1.9}$$

Because *I(z,t)* also satisfies the one-dimensional wave equation, it can also be written as the sum of travelling waves.

$$I = I_+(\alpha) + I_-(\beta) \tag{2.1.10}$$

Substitute equation (2.1.3) and (2.1.10) into either equation (2.1.5) or (2.1.6), we can get:

$$I = \frac{1}{Z_0}[V_+(\alpha) - V_-(\beta)] \tag{2.1.11}$$

Where:

$$Z_0 \equiv \sqrt{\frac{L}{C}} \tag{2.1.12}$$

If we consider the input wave as a sine wave:

$$V = Re\hat{V}(z)e^{j\omega t} \qquad\qquad I = Re\hat{I}(z)e^{j\omega t} \tag{2.1.13}$$

Using transmission line equations (2.1.6) and (2.1.7), we get:

$$\frac{d\hat{I}}{dz} = -j\omega C\hat{V} \tag{2.1.14}$$

$$\frac{d\hat{V}}{dz} = -j\omega L\hat{I} \tag{2.1.15}$$

Again because of the constant coefficients, these linear equations have two solutions, each having the form *exp(−jkz)*. Substitution shows that

$$\hat{V} = \hat{V}_+e^{-j\beta z} + \hat{V}_-e^{j\beta z} \tag{2.1.16}$$

$$\hat{I} = \frac{1}{Z_0}\left(\hat{V}_+e^{-j\beta z} - \hat{V}_-e^{j\beta z}\right) \tag{2.1.17}$$

At any location on the line, the impedance is found by taking the ratio of $\hat{V}$ and $\hat{I}$

$$Z(z) \equiv \frac{\hat{V}(z)}{\hat{I}(z)} = Z_0\frac{1 + re^{2j\beta Z}}{1 - re^{2j\beta Z}} \tag{2.1.18}$$

The reflection coefficient of the load:

$$r \equiv \frac{\hat{V}_-}{\hat{V}_+} \tag{2.1.19}$$

The reflection coefficient is defined as a number that quantifies how much electromagnetic wave is reflected by impedance discontinuities in the transmission medium. The reflection coefficient is the ratio of the amplitude of the reflected wave to the amplitude of the incident wave. It's a vector with phase information as well as shown above.

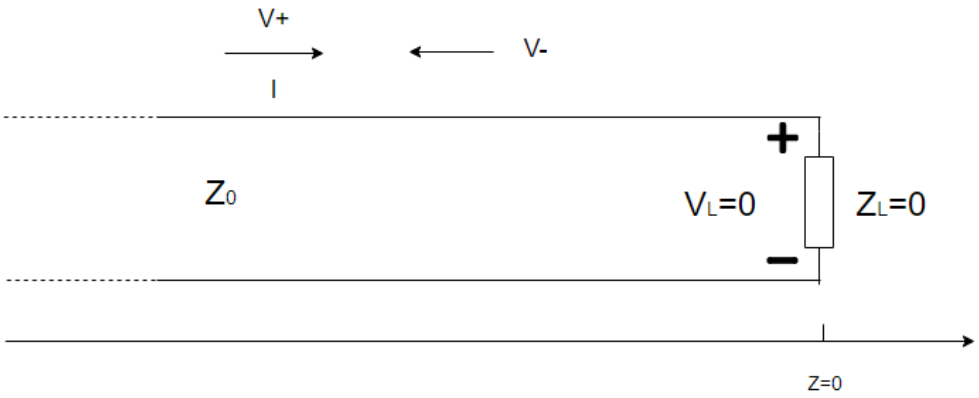

Figure 2 Representation of voltage wave on a transmission line. The voltage waves included two components V+ and V- representation waves propagating in positive and negative directions. Zo is defined as the characteristic impedance and Z_L is the load impedance.

At *z=0* where the line is connected to the load, this expression becomes

$$r = \frac{\frac{Z_L}{Z_0} - 1}{\frac{Z_L}{Z_0} + 1} \tag{2.1.20}$$

At a location z, the impedance of the transmission line is:

$$\frac{Z(z)}{Z_0} = \frac{1 + r(z)}{1 - r(z)} \tag{2.1.21}$$

$$r(z) = \frac{\hat{V}_-}{\hat{V}_+} e^{2j\beta z} \tag{2.1.22}$$

After determining the magnitude and phase of *Γ* at the load, the reflection coefficient can be obtained at another position by a simple rotation of *4π(z/λ)*. By mapping

impedance $\frac{Z}{Z_0}$ in the reflective coefficient r plane, we can infer the impedance implied by *r* elsewhere.

To this end, we define the normalized impedance as having the resistive part **a** and the reactive part **b**:

$$\frac{Z}{Z_0} = a + jb \tag{2.1.23}$$

Draw contours of constant *a* and constant *b* on the Γ plane. In this way, we can directly see the *Z* implied by each value of *r*.

These contour maps make up the *Smith chart*.

Below shows a Smith chart with $Z_L = 0$ and $Z_0 = 0$

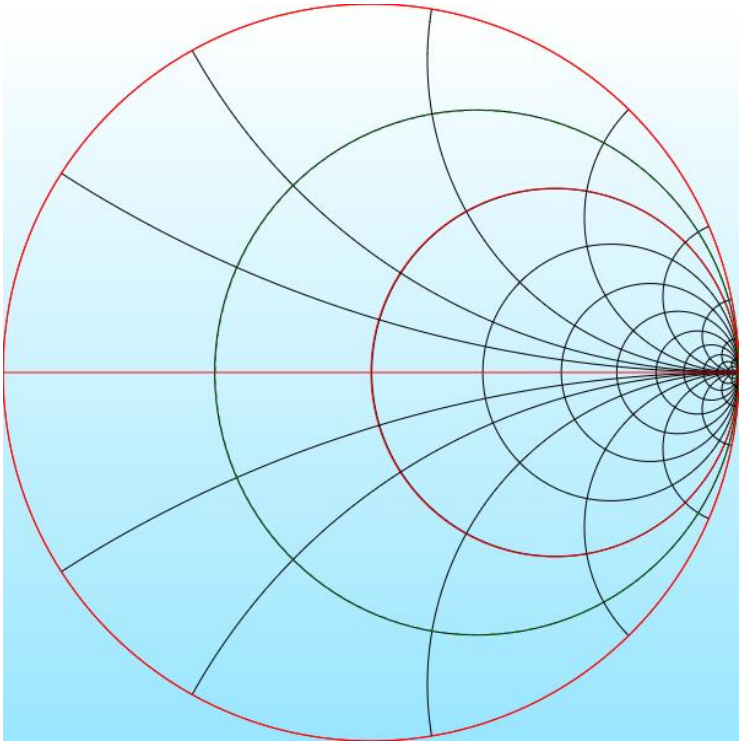

Figure 3 The Smith chart is commonly used in electrical engineering to represents complex reflectivity and wave impedance on the same figure. The centre of the graph is the zero reflection *r=0* which is the perfect impedance matching condition *Z=Z0*.

2.2 Transmission of electromagnetic waves

The description of the temporal and spatial evolution of the electric field on the

transmission line is also applicable to the description of electromagnetic waves.

Assume *E* has a component along the x-axis and *H* has a component along the y axis, using Maxwell's equation

$$\vec{E} = \hat{x}E_0 e^{j(wt-kz)} \tag{2.2.1}$$

$$k = \sqrt{w^2\mu\epsilon} \tag{2.2.2}$$

$$\vec{H} = \hat{y}H_0 e^{j(wt-kz)} \tag{2.2.3}$$

$$\nabla \times \vec{E} = -\mu \frac{\partial \vec{H}}{\partial t} \tag{2.2.4}$$

Where k is the wave vector, w is the frequency of the wave, μ is the magnetic permeability, ϵ is the electric permeability. Using equation (2.2.3) and equation (2.2.4), we know that:

$$\nabla \times \vec{E} = -\mu jw \;\; \vec{H} \to \vec{H} = \frac{\nabla \times \vec{E}}{-\mu jw} \to \vec{H} = \hat{y}\frac{-\mathrm{j}kE_0}{-ujw} e^{j(wt-kz)} \tag{2.2.5}$$

Coming back to equation (2.2.3) we can see:

$$\hat{y}H_0 e^{j(wt-kz)} = \hat{y}\frac{-\mathrm{j}kE_0}{-ujw} e^{j(wt-kz)} \tag{2.2.6}$$

$$H_0 = \frac{k}{wu}E_0 = E_0\sqrt{\frac{\epsilon}{\mu}} \tag{2.2.7}$$

$$E_0 = H_0\sqrt{\frac{\mu}{\epsilon}} \tag{2.2.8}$$

Compare with Ohm's Law, η which is the impedance of wave propagation, equals $\sqrt{\frac{\mu}{\epsilon}}$ and it's only related to the material of the medium.

When it comes to non-magnetic material, $\mu = \mu_0$

$$\eta = \sqrt{\frac{\mu_0}{\epsilon}} = \sqrt{\frac{\mu_0}{\epsilon_0}}\frac{1}{\sqrt{\epsilon_r}} = \sqrt{\frac{\mu_0}{\epsilon_0}}\frac{1}{n} = \frac{\eta_0}{n} \tag{2.2.9}$$

Where $\mu_0 = 1.2566 \times 10^{-6}$ H/m, $\epsilon_0 = 8.854 \times 10^{-12}$F/m, $\sqrt{\frac{u_0}{\epsilon_0}} = \eta_0 \approx 377\Omega$.

n is the reflective index of a material.

With reflective coefficient, $r = \frac{\eta_1 - \eta_2}{\eta_1 + \eta_2}$, in free space,

$$r = \frac{\eta_1 - \eta_0}{\eta_1 + \eta_0} = \frac{\frac{1}{n} - 1}{\frac{1}{n} + 1} = \frac{1 - n}{1 + n} \tag{2.2.10}$$

Let *A* be a set of complex numbers, and if, and there is a rule defined on A so that, there are one or more complex numbers *W* corresponding to any complex number *Z* in *A*, then a complex variable function is defined on the complex number *A*, recorded as *W = f (Z)*. If *z = x + iy, w = u + iv*, the complex function *w = f (z)* can be decomposed into *w = u (x, y) + iv (x, y)*; So a complex variable *W = f (Z)* corresponds to a real-valued function of two real variables.

Let's start with a simple single input and a single output, and if we want to solve for *f(x)=g(x)*, all we can think about is how these two functions intersect, and where their intersection is the answer. To determine where this point is, we can apply the intermediate value theorem. In mathematical analysis, the intermediate value theorem states that if the domain is a continuous function *f* of *[a, b]*, then at some point in the interval it can take any value between *f (a)* and *f (b)*. That is to say, the intermediate value theorem states that within an interval of a continuous function the value of the function must be between the maximum and minimum value. By narrowing the distance between the two points, we can keep narrowing the range of answers. In the same way, we can apply this idea to two-dimensional equations, where the inputs and outputs are both two-dimensional.

The other question is, in two dimensions, how do we define the position of the input and output values. One of the most effective ways to do this is to connect points in space with colours. So that's the chromatic scale. We can easily visualize the complex function by corresponding to the points of the same colour on the input and output

charts.

In the one-dimensional equation, we use two points to constantly narrow the range of the answer, but in the two-dimensional equation, we will use a closed curve to examine the boundary of a region. If the loop hits all outputs of possible colours on the boundary, we can say that somewhere inside the region, it must go zero. But what if neither region contains a zero, then combining their boundaries is just the right way to get a complete colour map? It is not accurate. So this leads to the winding number. The winding number around a point on a closed curve in the plane is an integer, which represents the total number of times the curve circumnavigates that point. The number of winding is related to the orientation of the curve. If the curve goes clockwise around a certain point, the number of winding is negative. If γ is a closed curve then its winding number about Z_0 is defined as:

$$W(\gamma, Z_0) = \frac{1}{2\pi i}\int_{\gamma} \frac{1}{Z - Z_0} dZ \tag{2.2.13}$$

With the help of winding number, this time we can say if the loop hits all outputs of possible colours on the boundary while this loop has a non-zero winding number, we can say that somewhere inside the region, it must go zero.

Since we found a way to solve complex functions, something is annoying which makes solving complex functions difficult, these are singularities. A singularity is usually a point when a mathematical object is said to be undefined, or when it is out of order in such a special case that the point appears in a set of exceptions. In singularities, the zeros and poles play an important role.

According to the Argument principle:

$$\int_{\gamma} \frac{f'(Z)}{f(Z)} dZ = 2\pi i \left(\sum_{k=1}^{n_Z} (Z_k) - \sum_{k=1}^{n_P} (P_k) \right) = 2\pi i W \tag{2.2.14}$$

Z_k means zero and P_k means pole. When the loop goes around the singularity. There's a 2π phase accumulation.

Since the reflective index is a complex number, then the refractive coefficient is a complex function. The pole and the zero for this function are -η_0 and η_0 respectively. At this point, the real part of the value is 0 but the imaginary part is unknown, therefore the singularity brings up a lot of interesting things.

$$r = \frac{\eta_1 - \eta_0}{\eta_1 + \eta_0} = \frac{\frac{1}{n} - 1}{\frac{1}{n} + 1} = \frac{1 - n}{1 + n} \tag{2.2.15}$$

In the complex plane using domain colour map in Figure 4:

Since we can't have a negative wave impedance in a classical lossy system, we can only achieve the zero point. The continuity of the function is destroyed due to the existence of this point (zero point), we can say that it is a singularity.

According to the definition, the complex analytic set is a Hausdorff topological space that can be covered by a set. The graphs of the set can be identified as the following model: there are zero-loci in the open subset of the holomorphic function set. In addition, we also require that the change of the holomorphic graph is also holomorphic. In this way, the concepts of holomorphic functions and holomorphic mappings from one complex analytic set to another complex analytic set can be easily defined. In particular, we can say holomorphic isomorphism, also called holomorphic equivalence.

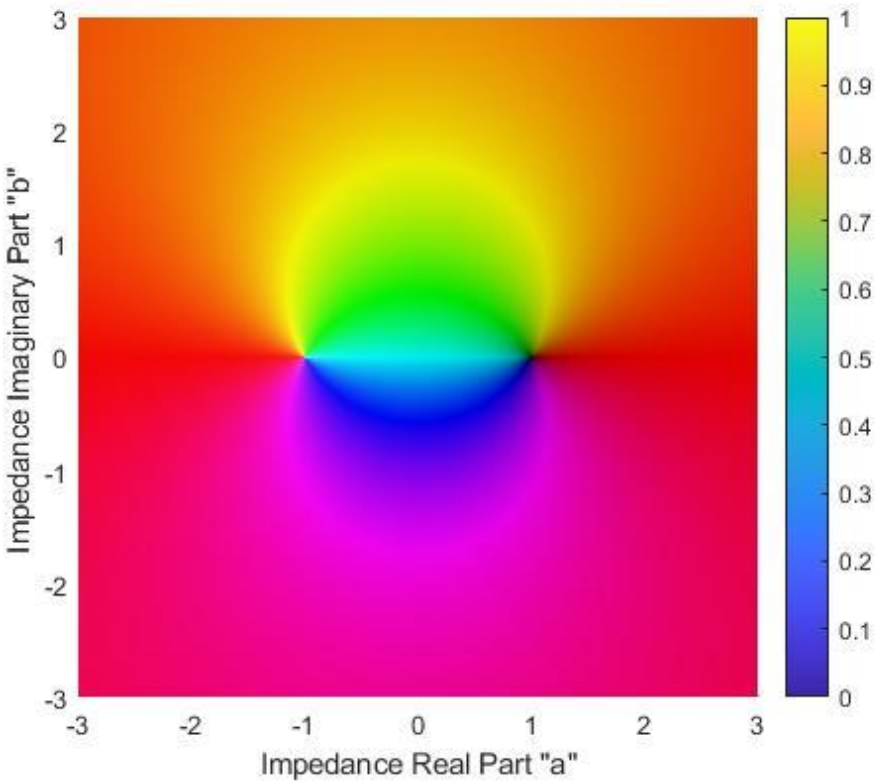

Figure 4 The colour map represents the phase of reflectivity as a function of complex impedance *Z*. There are two points where the phase is not defined *Z=Z0* and *Z=-Z0*. These two points are called phase singularity of topological defects with a topological charge of =1 and -1. These singularity points will have a key role in our experiments.

If two isolated singularities have representatives that can be identified by homomorphism sending one base point to another base point and keeping the direction (direction derived from the complex structure) outside the base point, it is called topological equivalence. How to encode a topological equivalence class of an isolated complex singular point? The usual method is to start with some of its representatives and define suitable tubular neighbourhoods of the base point, which are cones on a true smooth manifold, the boundary of the singular point or link. Therefore, the topological type of singularity can be captured by the topological structure of its boundary.

In combination with the previous analysis of two-dimensional functions, we can say that if two sets of two-dimensional numbers can be mapped to each other, they are topologically equivalent, and their winding numbers are the same.

Chapter 3 Topology and Photonics

3.1 The concept of topology

Topology is a branch of mathematics that deals with quantities that are maintained under continuous deformation. For example, each of the six objects in the figure has a different geometry, but only three different topologies. Spheres can be continuously transformed into spoons, so they are topologically equivalent. A torus is topologically equivalent to a coffee cup, and a double torus is topologically equivalent to a teapot. Different topologies can be represented mathematically by integers called topological invariants -- quantities that remain constant under any continuous deformation of the system. For the above-closed surface, the topological invariant is its genus, which corresponds to the number of holes in a closed surface. Objects with the same topological invariant are topologically equivalent; That is, they are in the same topological phase. The topological invariant changes only when a hole is created or removed from the object. This process is called a topological phase transition.

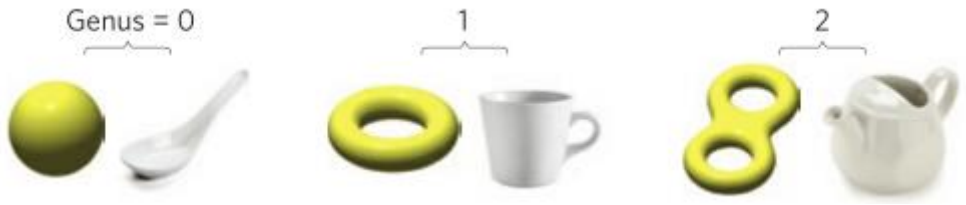

Figure 5. The concept of topology uses integer numbers to clarify geometrical objects. These integer numbers are called topological invariants which stays constant during continuous deformations. In the figure, the genus represents the number of hole on these geometrical objects which stays constant under continuous deformations. This idea of topology helps to simplify a complex problem into a simple one where the solution is obvious. After solving the problem on a simple topologically identical surface, the solution can be transformed into the initial complex configuration. The concept of topology has been implemented for a physical system to classify materials and optical systems based on the topology of the electronic or optical band structures [[2].

In a complex plane, the topological property of a closed loop is determined by the winding number of the loop.

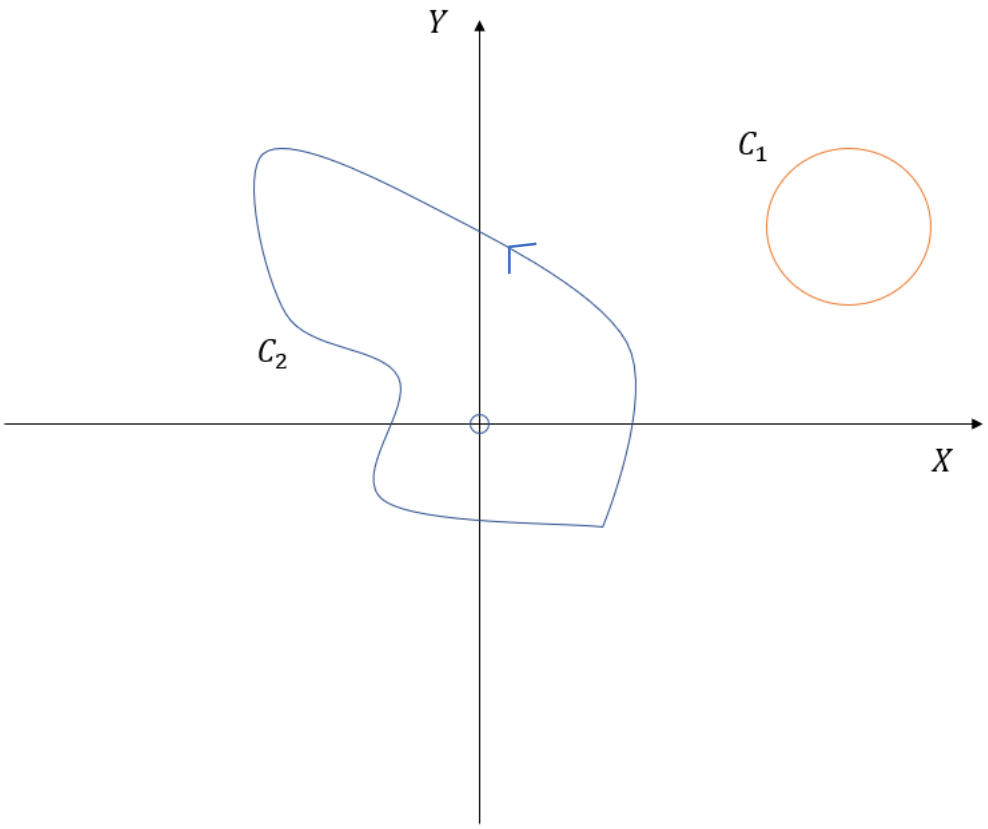

Figure 6 shows two closed loops C_1 and C_2 which are topologically different. Loop C_1 has a winding number of 0 and C_2 has a winding number of 1.

For example, here the winding number of C_1 is 0, the wingding number of C_2 is 1, they are topologically different.

Once a physical observable is written as a topological invariant, it can only vary discretely; therefore, it does not respond to continuous small perturbations or local errors. These perturbations may be any continuous variation of system parameters. The bulk-edge correspondence[[92]provides a deep physical meaning of topological invariants: when two materials with different topological invariants contact, there must be a spatially localized edge state at the interface where the energy is within the energy gap of the surrounding bulk materials. Bulk-edge correspondence can be understood heuristically in the following way: Under perturbation or deformation of the system, the integer topological invariant of a notched system cannot change its value unless the energy gap to the excited state closes somewhere. This means that when two materials

with different topological invariants come into contact, the energy gap in the interface region must close, resulting in the occurrence of local states in the region. In finite-size samples of nontrivial topological materials, the physical edge of the sample can be considered as the interface between the region with nonzero topological invariants and the topological trivial vacuum, thus ensuring the existence of local states on the system boundary.

3.2 Progress in topological photonics

In recent years, the topological properties of materials have become a hot topic in condensed matter physics and material physics. Topological physics involved in the quantum Hall effect and topological insulators has attracted the interest of researchers in many fields. Topologically protected edge states have been realized in many quantum and classical wave systems, such as condensed matter, optics and acoustics.

The original idea of topological photonics came from the topological phase of matter in solid-state physics, and the great development of this field began in 1980 when The Integer quantum Hall effect was discovered. [[3] In other words, the Hall conductance of two-dimensional electronic gas will appear as a platform related to magnetic field degree under vertical strong magnetic field, and its value is an integer multiple of e^2/h. In addition, this quantized Hall conductance is insensitive to carrier concentration and mobility and has certain robustness. Thouless et al. [4] and Kohmoto[[5] soon realized the importance of this discovery, and they correlated the integer occurrence of Hall conductance with the topological invariant of the system —— Chern Number, which is a topological invariant with an integer value. It describes the global configuration of the wave function in momentum space. Later, this method of combining topological invariants with the conductivity of quantum Hall effect is summarized as Thouless-Kohmoto-Nijs (TKNN) [[93] relation. The physical significance of topological invariants is embodied in the volume-edge correspondence of materials: in electronic systems with band gaps, integer topological invariants do not change due to perturbation or continuous deformation unless the band gap closes somewhere. This

means that when two materials with different topological invariants are spliced, the electrons at the interface will have a space field local at a specific energy, and the energy of the electrons at this time is in the bandgap of the bulk material. If topological nontrivial materials are of finite size, this splicing interface can be understood as the interface between topological nontrivial regions and topological trivial regions (e.g., vacuum or topological trivial materials with zero ordinary topological invariance), thus ensuring that the system interface has local boundary states.

In 2005, Kane and Shousheng Zhang et al. proposed that a pair of conjugated spin-opposite gapless boundary states, namely quantum spin Hall effect (2D) or topological insulator (3D), could also exist in a zero magnetic field by using spin-orbit coupling [[6-[7].

At this point, the total Hall conductance is zero, but the spin Hall conductance is non-zero, which can be described by Z2 topological invariant or the spin Chern number (Cs), and the system has the spin transport property of symmetric protection of time inversion. When the material or lattice parameters are changed with the same topological properties, the boundary states of ordinary insulators must have an energy gap and are symmetric, while the topological boundary states of quantum Hall and quantum spin Hall effect do not open an energy gap.

By applying the mathematical concept of topology to the photonic crystal band theory, similar quantized topological states can be realized.

The combination of the concept of the topological phase of condensed matter and the optical system gives birth to a series of novel optical physical phenomena and potential optical application prospects. These physical phenomena, such as the optical integer quantum Hall effect [[8-[11], the optical quantum spin Hall effect [[12−[16], and the optical Floquet topological insulator [[17−[26], have boundary states protected by topology and suppressed by backscattering. It has a broad application prospect in optical transmission [[9,[12,[27,[28] and optical quantum computing [[25,[29−[31] and

thus has become a hotspot in the field of photonics.

In these novel research directions, firstly, it is not very difficult to introduce the gain loss of materials in optical systems. It is necessary to consider the gain loss in many cases (such as optical transmission and coupling systems), which has triggered the research on non-Hermitian topological photonic systems [[32−[47]. Secondly, the nonlinear process has been a topic in the field of optics for a long time. As the concept of the topological phase is well known to more and more people, topological configurations with nonlinear optical effects come into being and develop towards richer contents [[20,[24,[48−[58]. Third, although the concept of higher-order topological phases originated from the tightly bound model of electronic systems, it has attracted more and more attention in the field of photons because it is possible to realize local field manipulation with topological protection [[59−[73].

After introducing some basic concepts in the field of topological photonics, I will start from the dimension of topological photon systems: Topological description method and application of Su-Schrieffer–Heeger (SSH) model in one-dimensional system, optical integer quantum Hall effect in two-dimensional system, optical quantum spin Hall effect and Floquet topological insulator. In addition, the non-Hermitian topological photonics, nonlinear topological photonics and high order topological insulators are briefly introduced and discussed given the current development trend of topological photonics.

3.2.1 One dimensional topological photonic system

The topological phase regulation of one-dimensional ordered structures is inseparable from the regulation of symmetry, among which chiral symmetry is the most important or widely discussed one. The most representative model is the SSH model proposed by Su et al. [[74] in 1979.

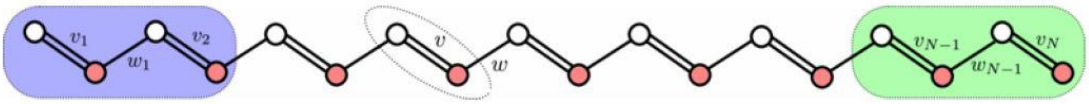

Figure 7 Schematic diagram of SSH model, each cell contains two lattice points. [91]

Depending on the dimerization, the winding number W can have two possible values: 0 when $v > w$ and 1 when $v < w$. These two windings correspond to two different topological phases of the system. In an infinite lattice, the difference between the two cases does not matter, because it depends only on the choice of cells that define v and w. However, in semi-infinite chains, the unit is explicitly defined by terminations that set the chain's winding. When W =0, the lattice is topologically trivial and no edge state is expected, but when W = 1, the lattice is topologically nontrivial and the topological state is on the edge is expected. Similarly, when two semi-infinite SSH chains with different windings are connected, a local interface state occurs [[75].

In 2017, St-Jean et al. [[76] observed the generation of laser on one-dimensional topological boundary by using micro-nano manufacturing technology. As shown in Figure 8(a), the quantum well is placed in the distributed Bragg reflection micro-cavity by micro-nano manufacturing. The coupling between the two dipole modes P_X and P_Y of a single column is used, as shown in Figure 8(b). From Figure 8(c) the local boundary states are observed in the bandgap between the two bands of P state and the laser excitation is realized. In 2018, Parto et al. [[77] designed and experimentally prepared a micro-ring resonator array based on the SSH model, and realized the excitation of boundary states. As shown in Figure 8(d), corresponding local boundary states can be obtained in the coupled waveguide of the boundary through up-down coupling waveguide channels.

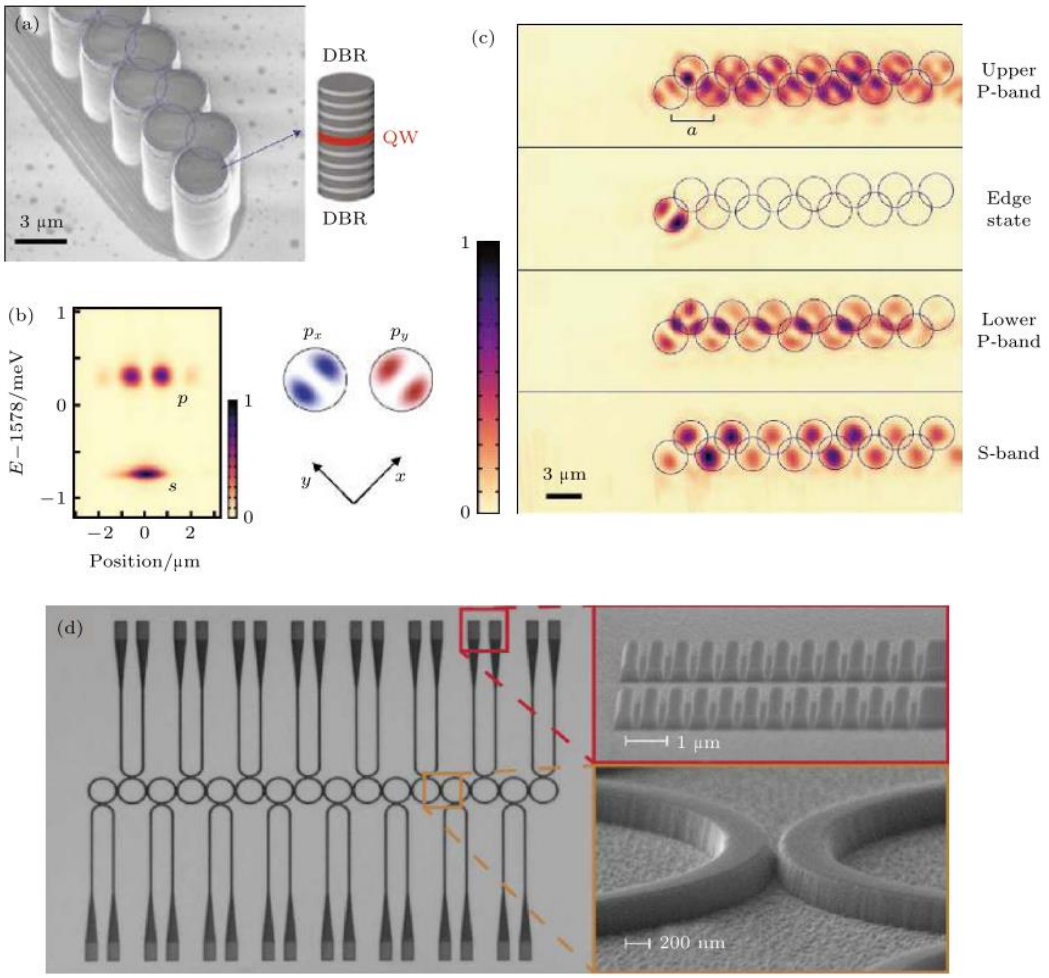

Figure 8 (a) Images of micro-nano machining (SSH model); (b) Patterns of individual columns; (c) States in different energy bands and existing boundary states; (d) Using waveguide annular array to realize SSH model [76][[77]

The topological properties of the SSH Hamiltonian are very convenient for designing structures with isolated states in the middle of gaps. In addition, these states are remarkably robust to certain types of disorders. The topological properties of SSH Hamiltonians are closely related to the chiral symmetries of the above Hamiltonians, as the Hamiltonians are purely non-diagonal. The main result of chiral symmetry is that the spectrum is mirror-symmetric with respect to E = 0: every eigenstate of energy E has a partner eigenstate of energy -E. The topological edge or interface state at E = 0 must be its companion, and thus its energy is insensitive to any modification of the Hamiltonian that preserves chiral symmetry. In particular, the disorder in bond between

v and w preserves this symmetry and does not affect the energy of the topological state as long as the gap between the two bands is clearly defined. In contrast, the energy of the edge mode is protected from disturbances that break the chiral symmetry.

3.2.2 Two dimensional topological photonic system

3.2.2.1 Photonic Integer Quantum Hall Effect in two dimensional topological optical systems

The integer quantum Hall effect of light is derived from the experience of condensed electron-gas system.

In 2005, Haldane and Raghu of Princeton University proposed that a boundary state of transverse electric polarized light could be constructed in triangular or hexagonal spin photonic crystals by breaking the time-reversal symmetry with external magnetic field. This leads to the Dirac point degeneracy open in the optical band structure, i.e. the optical analogy of integer quantum Hall effect [[8]. This boundary state can completely suppress the backscattering so that the electromagnetic wave can only propagate in one direction.

Subsequently, the MIT team experimentally observed for the first time the backscattering suppressed single-pass topological photonic state of transverse magnetic(TM) polarized light [[10], in which the vanadium-doped Ca-Fe garnet cylinder was used to break the symmetry of the time inversion. Under an external magnetic field ($0.20T$) and at a frequency of about $4.5GHz$, the amplitude ratio of forwarding propagation and backward propagation of chiral boundary states is greater than 50 dB, showing the robustness of defect immunity and one-way propagation around obstacles, as shown in the figure 9.

Due to the low frequency of magnetic response, the realization of optical quantum Hall effect based on gyromagnetic materials is generally limited to the microwave band (gyroelectric materials are at most to the infrared band), so it is difficult to be applied in the infrared and even visible light.

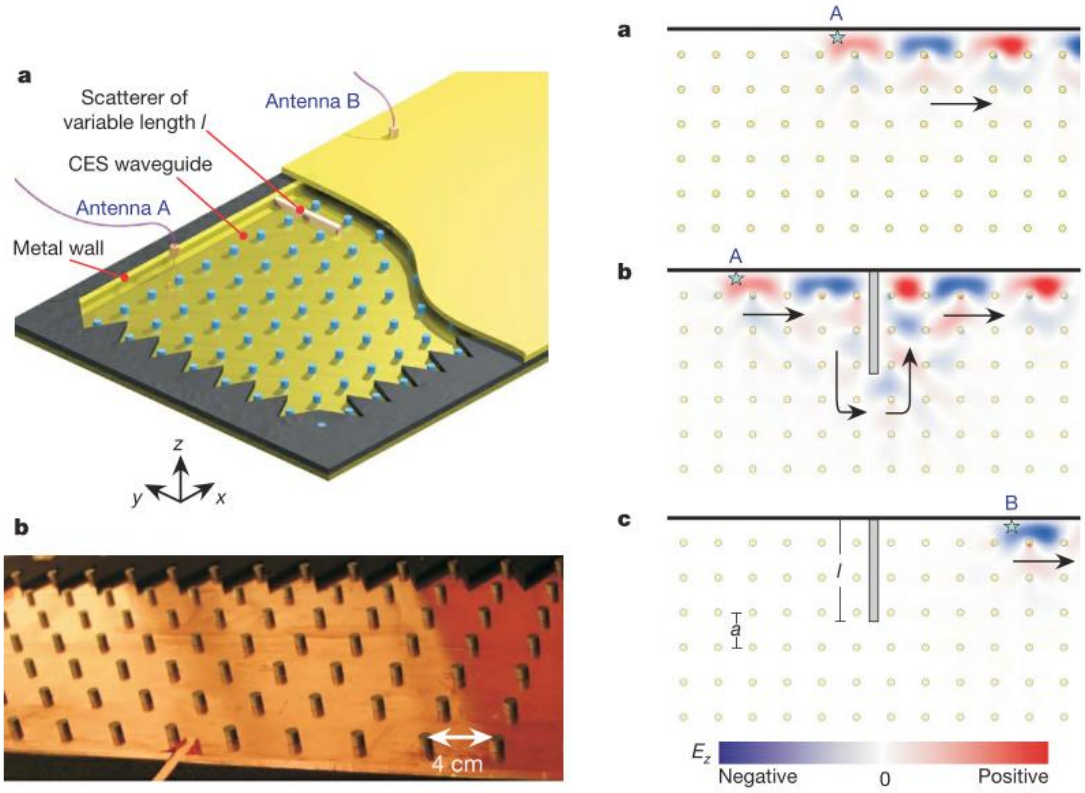

Figure 9 left a and b: Schematic of the waveguide composed of an interface between a gyromagnetic photonic crystal (PhC) slab (blue rods) and a metal wall (yellow). Right a, b, c: unidirectional backscattering-immune result.[[10]

3.2.2.2 Photonic Quantum Spin Hall Effect in two dimensional topological optical systems

Another major category in topological photonics is quantum spin Hall effect systems that preserve the symmetry of time inversion or pseudotime inversion. For the electronic system, since the electron itself has + or - spin, for each spin S, a Chern number $C_{\uparrow}$ and $C_{\downarrow}$ can be separately specified to represent the band with the corresponding spin. Therefore, topological invariants can be used in two-scale signs, one is the traditional Chen number C, the other is the spin Chen numberC_S .

Since the system still has time inversion symmetry in a broad sense, the Chern number C = 0, while the spin Chern number Cs is an integer value, which can be used to describe the quantum spin Hall effect. It is worth noting that in the case of only time inversion symmetry, the spin number no longer has a clear definition and can be replaced by

topological invariants.

The spin of the photonic system is very different from the intrinsic spin of the electrons. At present, there are three main schemes to realize the spin Hall effect of the photon.

The first scheme is about using degree of freedom of polarization of photons. In 2016, He et al. [[78] proposed a photonic crystal model based on piezoelectric-piezomagnetic superlattice, and took left-handed and right-handed light as pseudospin states, as shown in Figure 10(a). The model adopts a tetragonal lattice configuration and ensures that the time reversal symmetry is broken. However, the symmetry of the electromagnetic coupling reversal and time reversal (pseudo-time reversal symmetry) is preserved. Thus confirming that the time reversal symmetry itself is also only for the inherent electric field and magnetic field system, even if the time reversal symmetry is broken, the photon spin Hall effect can still occur. As shown in Figure 10(b), when the selection of (pseudo) spin states changes, the corresponding (pseudo) time inversion symmetry operator may also change, which plays a great role in understanding the role of time inversion symmetry in the spin Hall effect of optical quantum spin hall effect.

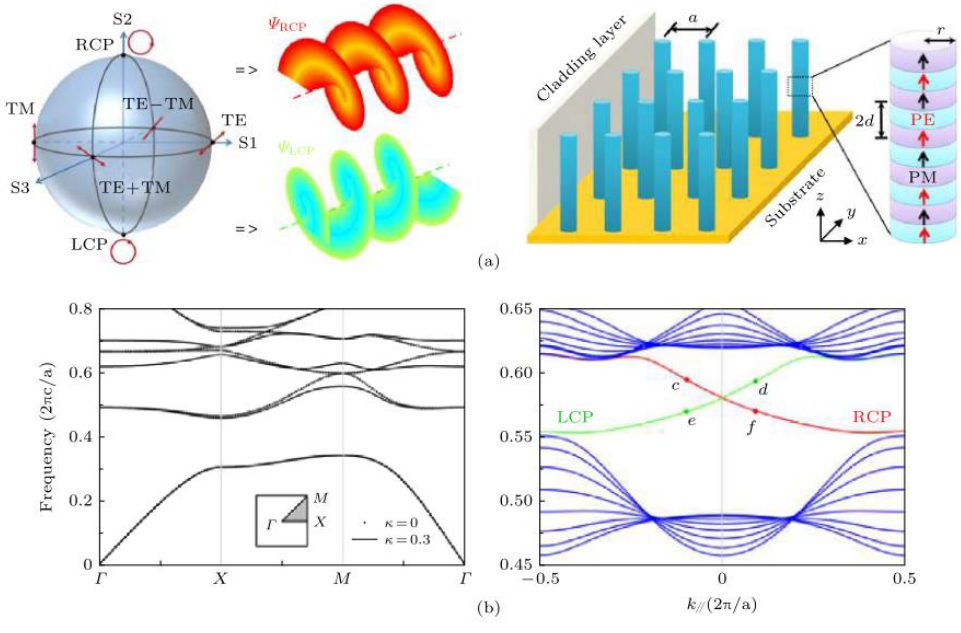

Figure 10 (a) Left circular polarization and right circular polarization on Poincaré spheres, as well as photonic crystals composed of piezoelectricity and piezomagnetic materials; (b) The absence of pseudo-spin coupling and the band with pseudo-spin coupling and the projection band of the latter.[[78]

In addition to considering the degree of freedom of polarization to simulate the electron spin, the pseudo-time inversion symmetry can be constructed by designing the symmetry of crystals (which can be regarded as a kind of topological crystal insulator), and the mode degrees of freedom between optical Bloch states can be used to simulate the electron spin. Demonstrated in figure 11, NIMS researchers in Japan theoretically proposed that optical quantum spin Hall states based on Bloch state mode hybridizations can be constructed through the *C6* rotational symmetry in the compound hexagonal lattice [[13]. This design does not need to consider the complicated polarization coupling and is more conducive to the construction of optical topological insulators using pure dielectric photonic crystals.

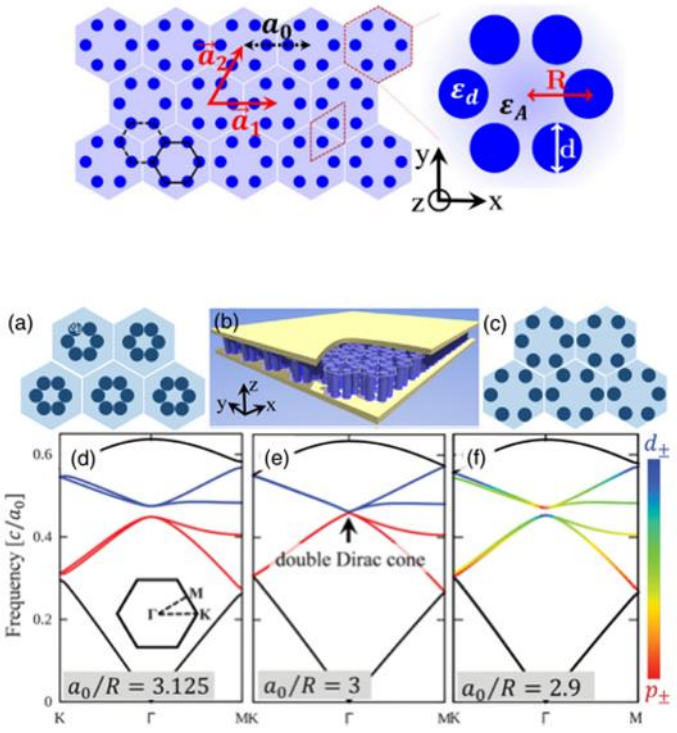

Figure 11 A Photonic crystal with hexagonal lattice used to demonstrate a topologically trivial and nontrivial crystal by deforming the position of the pillars in the radial directions. The band structure of the photonic crystals for 3 different cases. For a perfect hexagonal lattice there is no photonic bandgap, however, when the pillars are deformed in the radial direction a topologically different bandgap can be opened.[[13]

The third scheme is realized by coupling light into a ring resonator array system. By controlling the path of light travelling clockwise and counter-clockwise along the

resonator array, the system is given a degree of freedom to control the transmission of light, which is analogous to the spin of an electron. Since such a system naturally preserves the time-reversal symmetry and it can be analogous to the quantum spin Hall effect.

In 2011, researchers from the University of Maryland proposed a theoretical design[[79], and then (2013) experimentally implemented a unidirectional boundary propagation state related to the clockwise and counter clockwise propagation modes of the ring resonator array based on the directional coupling of the resonant coupling loops on two lattices[[80].

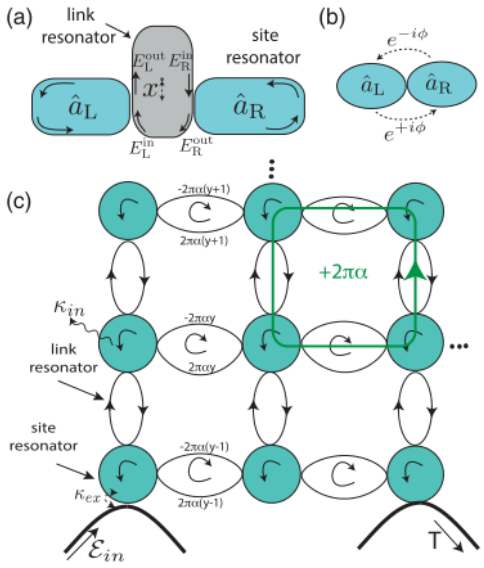

Figure 12 Coupled ring resonators which acquire different phase depending on the coupling direction. (a) Couple two adjacent resonators through a waveguide; (b) There is a non-zero hopping phase ϕ between the two adjacent resonators; (c) Putting an asymmetric coupler between the resonators provide a different optical path for light in CW and CCW directions. Through the resonant cavities periodically arranged in a two-dimensional plane Realize the Harper-Hofstadter model.[79]

As shown in the figure above, the clockwise (counter-clockwise) mode of propagation through a small cell produces an effective gauge potential with the opposite sign. These two modes of light, analogous to the "spin" of an electron, travel in one direction around the boundary. The unidirectional transmission of communication band light (1539 nm) and the absence of reflection bypassing the lattice defect are verified experimentally. This structure based on resonantly coupled microcavity can completely correspond to

Floquet topological insulator in the mesh model. It should be noted that in these two types of models, the two optical pseudospins are completely decoupled, so the defect-immune properties of this topological state are limited to the case of no spin reversal.

3.2.3 Floquet topological insulator

By introducing time modulation or method equivalent to time modulation into the Hamiltonian, materials can also generate novel topological properties. This class of topological insulators is commonly known as Floquet topological insulators.

In 2013, researchers at the Israel Institute of Technology proposed a scheme to generate an effective gauge potential (or an effective magnetic field) employing spiral modulation in the spatial dimension (Z direction), to achieve an optical Floquet topological insulator experimentally [[22,[81,[82]. The topological boundary states of the gaps can be obtained.

The experimental results show that light (633 nm) can propagate around its boundary in the Z direction without backscattering (one-way spiralling) and has certain immunity to defects.

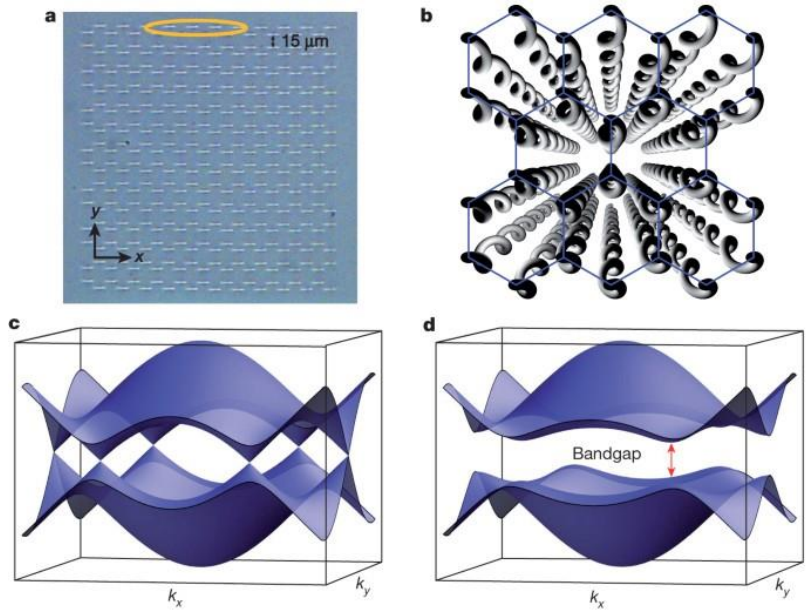

Figure 13 Topological photonics using coupled waveguide arrays. Twisting the waveguide along the propagation direction mimics the breaking of time-reveal symmetry by the magnetic field.[22]

3.2.4 New topological effects in photonics

3.2.4.1 Non-hermitian topological photonic effects

Gain and loss in photonic systems have long been the focus of researchers. The combination of the traditional control methods in these photon systems with the topological research of condensed matter physics has led to the extensive study of non-Hermitian photon systems. At present, the research of light transmission in Non-Hermitian topological system can be divided into two aspects: first, topological system with a gapless mode; Second, topological systems with energy gaps. For Non-hermitian topological systems with no energy gap in photon band diagram, people mainly focus on exceptional point [[83], exceptional rings, skin effect [[37] and other physical mechanisms that have novel regulatory effects on the transmission of light in non-Hermitian photonic bulk materials. At the same time, because the optical system has the advantages of easy control, less impurity and easy preparation, it has great advantages to study non-Hermitian phenomena in quantum mechanics by using optical system.

Based on this theory, Zhao et al. proposed a method to realize topological light transmission through non-Hermitian modulation in Hermitian optical topological insulators. [[84] This is done by performing optical pumping in part of an optical topological lattice composed of InGaAsP, resulting in gains (through external pumping) and losses (intrinsic material losses without pumping), as shown in Figure 14. The gain (fundamental to lasers) and loss is a characteristic of an optical system that allows the system to be represented by a non-Hermitic Hamiltonian, which has no direct correspondence in electronic topological insulators. When gain-loss contrast exceeds exceptional point (EP, the position of the non-Hermitic Hamiltonian with coalescing eigenstates), the new topological boundary states are observed at the boundaries of the gain and loss regions. This method does not change the topological properties of the photonic lattice, but only designs specific pumping patterns on the photonic lattice and then performs non-Hermitian regulation. At the same time, light can travel along any

path in this way, completely using the space of the photon lattice.

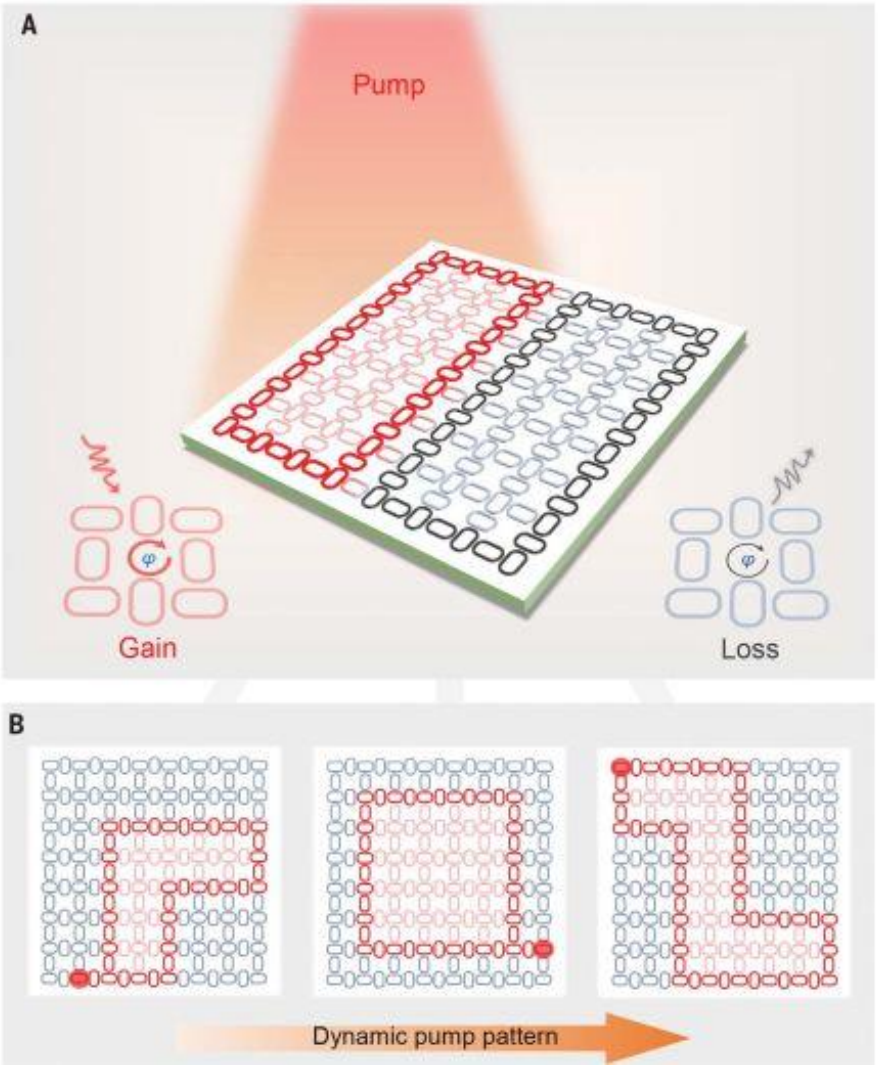

Figure 14 Non-hermitian light regulation in topological micro ring lattices. (a) A partial area of the optical topology lattice composed of InGaAsP is optically pumped, thereby generating gain (through external pumping) and loss (intrinsic material loss without pumping) (b) A specific pumping pattern is designed on the photonic lattice, and the new topological boundary state is observed at the boundary of the gain and loss regions. [[84]

3.2.4.2 Nonlinear topological photonic effects

Nonlinear optics is an important branch of modern optics, which is of great significance to the development of spectrum technology, imaging technology and optical information processing technology. The semi-classical nonlinear process can be

realized by introducing nonlinear terms into Maxwell equations and is the result of the

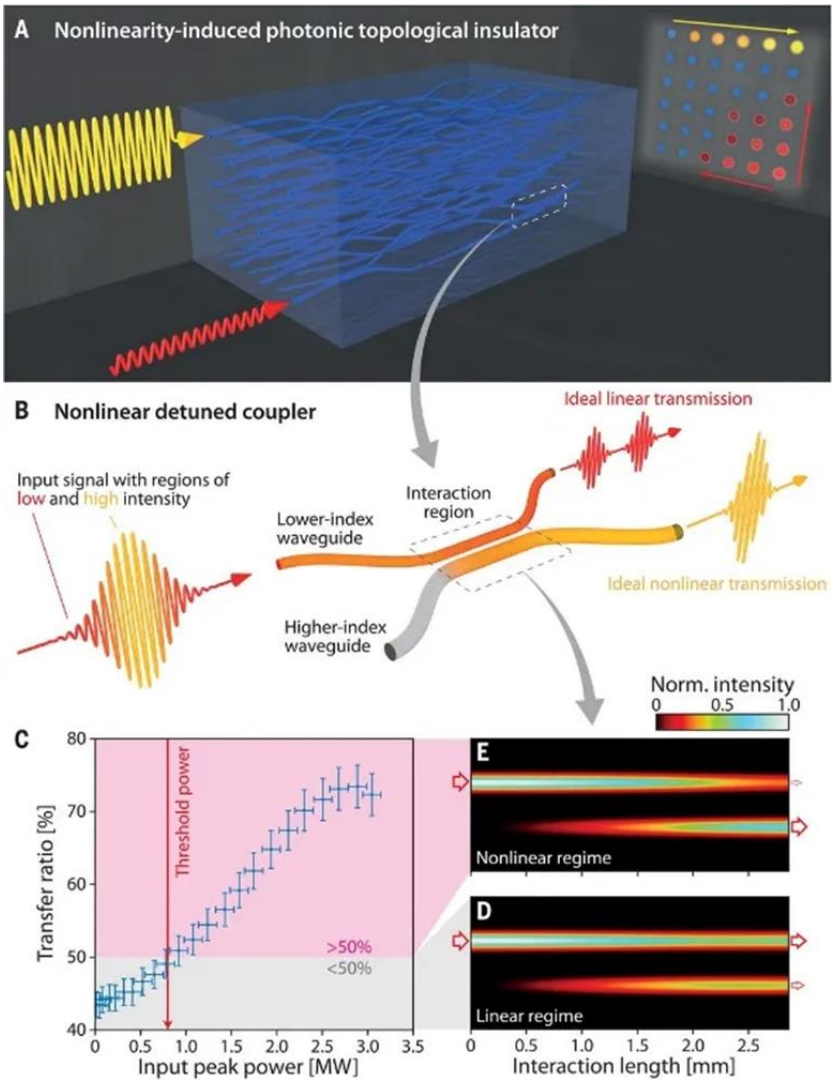

Figure 15 Nonlinearity-induced photonic topological insulator and its regime. (a) Non-linearity induced photon Topological insulator. The low-power edge excitation (red) undergoes diffraction, indicating that the topology is trivial. In contrast, high-power light (yellow) produces self-guided unidirectional edge states that propagate along the perimeter of the structure. (b) Nonlinear directional detuning coupler. The intense laser pulse is launched into the low-index waveguide (smaller diameter) of the detuned coupler. Focusing Kerr nonlinearity allows the high-intensity part of the pulse to temporarily compensate for the detuning, thereby transmitting light to a higher index waveguide (larger diameter). In contrast, the lower intensity part exhibits linear dynamics and remains in the lower index waveguide. (c) Power dependent transmission ratio measured in detuned coupler (d) and (e) Simulation of light transformation in this detuned coupler with different intensity respectively. [[85]

nonlinear response of the electric polarization vector to the electric field. Combining the concept of topology and nonlinearity, may enable the generation of topological mott insulators, topological insulators generated by interactions (such as Kondo and non-Abelian topological insulators), and may even drive the formation of topological solitons. Nonlinear optical topologies can change their topological properties by changing light intensity and can break optical reciprocity to achieve full topological protection.

In view of this, Professor Alexander Szameit studied the topological properties of matter in nonlinear states [85].In figure 15, using the photon platform, optical nonlinearity can cause topological changes in the lattice properties of photons. We demonstrate theoretically and experimentally the nonlinearity-induced generation of photonic topological insulators, showing how nonlinearities drive an initial topological system into a transient topological phase where probe light is confined to propagating along the edges of the structure. At low excitation power, the probe light leaks evenly into the rest of the lattice, an optically insignificant phase. Above the threshold power, optical nonlinearity results in changes in the topological properties of photonic lattices.

3.2.4.3 Higher order topological photonic effects

It is generally considered that the topological boundary state of an *N*-dimensional topological photon system is *N-1*, which makes our control of the local field dimension very limited. Recent studies have shown that some topological insulators have *N-1, N-2…N-M-1* dimensional energy-gap boundary states up to the last dimensional *N-M* boundary state, which is called m-order topological insulators. This idea is constructed by tight-binding model in condensed matter physics [[62],

Recently, Wang et al. [86] have experimentally demonstrated a higher-order topological bound state in a continuous medium. Specifically, they demonstrated two methods for identifying bound states in continuous photonic lattices: single point and superposition state injection. The team demonstrated that angular states located in a continuum and co-existing with scattered waves can be excited well. In a tightly bound two-dimensional Su-Schrieffer-Heeger (SSH) lattice, the second-order topological angular states are fixed at zero energy levels and embedded in the bulk mode. Intuitively, it seems that such angular states cannot be directly excited or observed. However, the team found that these angular states are orthogonal to the bulk mode in A Hilbert space, which makes it possible to excite them independently.

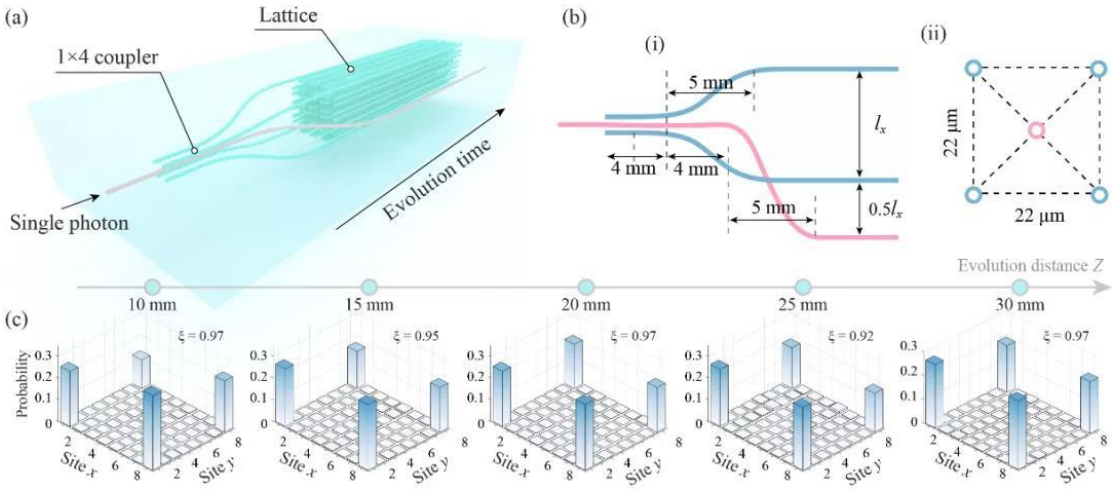

Figure 16 A quad-coupler and the measured angular photon distribution probability. (a) Schematic diagram of photon lattice. A four-part coupler is designed in front of the lattice. (b) Structural details of section (I) and side section (II) of a quad-coupler. (c) Experimental results of angular states obtained by excitation lattice with single photon superposition states. [[86]

As shown in the figure 16, they injected photons into a three-dimensional one-into-four photon coupler to create a four-input photon superposition state in the same phase and then injected the resulting photon superposition into the four corners of the lattice. Since the distribution probability of the photon in the lattice is the same as that of the zero-energy angular state in the same phase, the system is excited to the zero-energy angular state during the injection. Due to the orthogonality between the eigenstates, the photon

superposition state in the lattice can be maintained, which means that a single angular state is excited. The photon distribution probability measured in the experiment also shows that the photon output probability distribution follows the angular distribution and does not change with the evolution distance. Thus, the target zero-energy angular state is exited successfully by making the initial state of the system into its zero-energy angular state eigenwave function.

Compared with the electron system in condensed matter physics, the photon system has higher degrees of freedom in both structural design and regulation mode. In some aspects, it can construct a more perfect physical model and measure more abundant physical quantities compared with other natural material systems. Therefore, topological photonics has become an important platform for studying topological physical mechanisms. Furthermore, from the perspective of light field manipulation, boundary states with topological protection and backscattering suppression and higher-order topological states have great basic research and application prospects in optical transport, field dimension regulation and quantum optical transport.

The topological photonics field is, of course, facing some challenges. On one hand, the challenges for photonic devices, integrated topology band of photonic devices combined with existing silicon-based semiconductor process will have greater prospects in the direction of optical communication, optical computing, however infrared and even shorter wavelength band makes topological photonic devices need to do smaller, this is subject to micro/nano machining technology and topological structure design. On the other hand, the tenability of the devices. The construction of a tunable topological photonic system is limited by the characteristics of materials. This can be regulated by thermo-optic, electro-optic, phonon-optic and magneto-optic methods. However, they have various limitations in modulation rate and modulation amplitude.

In addition, there are theoretical and design challenges, for example, there are still many problems that need to be studied in non-Hermitian systems, three-dimensional (or higher dimensional) photonic topological insulators and higher-order topological insulators.

Chapter 4 Topology and geometrical phase

4.1 Topology in Surface plasmon polaritons

Surface plasmons are electronic resonance phenomena generated at the interface of positive and negative dielectric constant materials under the excitation of incident light. This phenomenon occurs when the wave vector of the incident light matches the electronic oscillation frequency of the inner surface of the metal, and the near-field field strength increases at the resonance wavelength. This near field is highly concentrated in the nanoparticle and decays rapidly as it enters the dielectric substrate away from the nanoparticle/dielectric interface. Surface plasmons are very sensitive to changes in the refractive index of the metal surface, and various sensors based on this principle have received extensive attention.

As shown in the figure below, when light goes through a prism, the reflection happens at the interface between metal and prism. When the incident Angle (resonance Angle) increase so that the photon energy and metal surface plasmon excitation energy is the same in this system, electronic absorption of photons happens because of the light-matter interaction from metal film, leading to resonance. The resonance is electronic surface plasmons. The result of surface plasmon resonance is a loss of the intensity of the reflected beam, which appears as a dark band on the detector.

Prism coupling includes two configurations: one is the Otto structure(a): there is a gap between the prism with a high refractive index and the metal. The width of the slit is relatively small, about tens to hundreds of nanometers, which is not convenient to use, so it is only used occasionally in the process of scientific research. The other is Kretschmann structure(b): metal film directly plated on the prism, the incident light at the interface between metal - prism total reflection will happen, The evanescent wave of total reflection may match the wave vector of the surface ablation wave, and the energy of the light can be effectively transferred to the surface state, thereby generating the surface evanescent wave.

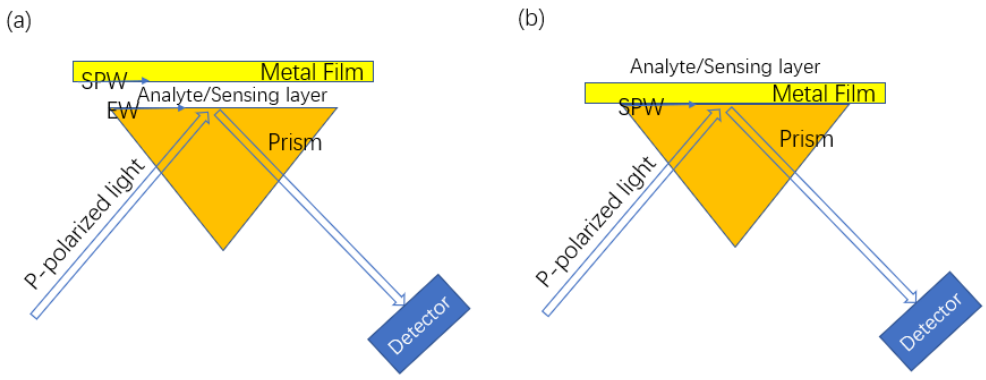

Figure 17 Two different configurations were used to excite surface plasmon polaritons. (a) shows Otto configuration where the plasmons are excited with evanescent filed in the gap between metal and prism surface. (b) shows the Kretschmann configuration where the SPP is excited on the metal-air interface by the evanescent field in the metal.

4.2 Geometric phase

The term "phase" is commonly used in physics and engineering to describe certain properties of oscillating systems, such as the phase of alternating current, the phase of vibrating strings, the phase of the wave function in quantum mechanics, and so on. This phase is called the kinetic phase ($\theta=\omega t$) which provides the time evaluation of the periodic system. After one period, the system accumulates a 2π dynamic phase which returns the system to the initial conditions. There is another type of phase which is related to the history of the system, more specifically where the particle has been. Intuitively, if a system is controlled by slowly varying parameters, we would expect the system goes back to the initial state when the parameters are returned to the initial values. For special cases, however, the system may accumulate an additional phase which is known as the geometrical phase. For example, if a particle goes through a closed-loop and comes back to the starting point, it may accumulate an additional phase depending on its path. Although it looks only an additional phase that does not affect observable physical quantities, it has interesting consequences: when the particle moves

on a path, this geometrical phase is related to the properties of the area covered by the path. Knowing the local forces on the path is not enough to find the final state of the system. Besides the local forces acting on the particle, there are additional nonlocal effects that provide this geometrical phase. Starting from the early days of quantum physics, the geometrical phase has been observed in many different classical physical, optical and quantum physical systems. Below, I would like to give some examples.

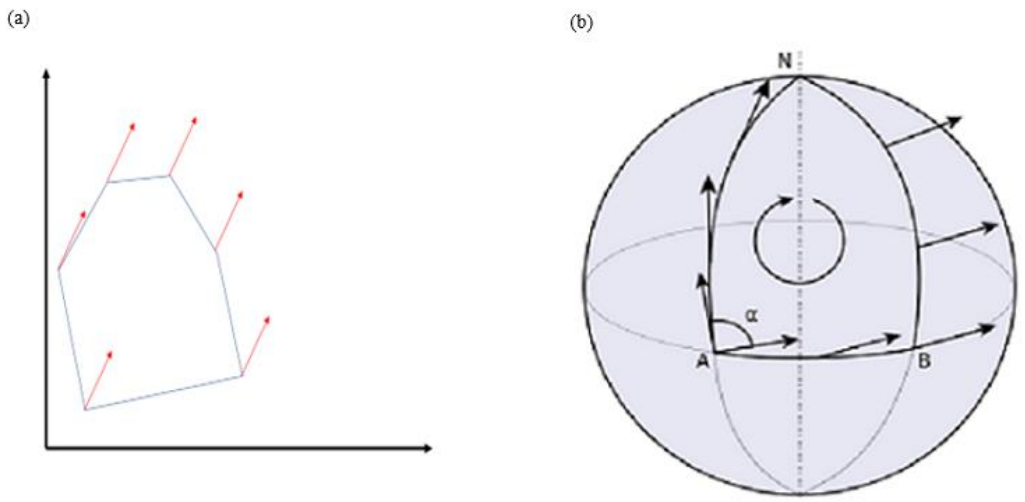

Figure 18 Transporting a vector on parameter space. a, A vector is transported on a cartesian parameter space, where the vector goes back to the original state. However, if the vector is transported on a surface of a sphere, the vector will accumulate an additional phase. In the figure, the vector starts from point A and goes to B and N then returns to A. After this transport on a closed cycle, the vector is rotated by an angle alpha which is related to the solid angle of the path on the sphere. This phenomenon has a good explanation in the parallel transmission theory.

Parallel transport is the key mechanism to understand the geometrical phases. Here a system is controlled by at least 2 parameters which define a multidimensional parameter space. When the parameters are changed slowly, the system moves on the parameter contour lines, this is called parallel transport. Figure 18(a) shows the parallel transport of a vector on a flat space and curved space on the surface of a sphere. As the vector is transported through a closed-loop on a flat parameter space (no curvature), it goes back

to the initial state without any phase accumulation or rotation. However, if the vector is transported on a curved parameter space, for example on a surface of a sphere shown in (b), when it comes back to the initial parameters, the vector rotates concerning the initial orientation. This rotation is the geometrical phase which appears as a rotation on the parameter space. In classical mechanics, this rotation is known as Hannay Angle [[87] which proves the existence of geometric phase even in classical systems.

The most classical example in physics is the Foucault pendulum. The Foucault pendulum is popular because it is a straightforward indication that the Earth is rotating. At first glance, the pendulum appears to swing back and forth along a line that runs through the centre of its disk. However, anyone who had watched for a few minutes would have noticed that the pendulum's path would slowly change and that it would rotate around the disk like the minute hand of a watch. But the pendulum itself has not changed direction. The earth is spinning under a free-hanging pendulum. If the Foucault pendulum were placed at the North Pole, it would appear that the pendulum's oscillations would rotate a full 360 degrees as the earth rotates over 24 hours, returning to its starting position by the end day. If the pendulum were hung at the South Pole, it would appear to rotate in the opposite direction. One particular aspect of the pendulum's motion didn't seem to bother anyone in Foucault's day, but it would have far-reaching consequences. If a pendulum were installed at the North Pole, the direction of its swing would rotate 360 degrees in a day. However, a pendulum placed at the equator does not rotate at all. In both cases, the pendulum ends the day swinging back in the direction it started. But when a pendulum is placed at a mid-latitude, the pendulum rotates less than 360 degrees during a day. Foucault's alignment is therefore an example of showing a geometric phase. After a complete closed cycle, the pendulum accumulates a rotation. The basic geometry of the earth is such that the pendulum eventually returns to the same place, but the pendulum does not move in the same way it did when it started.

The second example for the geometrical phase is from optics. As early as the 1860s, Maxwell had shown that light is an electromagnetic wave, consisting of electric and

magnetic fields oscillating together perpendicular to the direction of the wave's propagation. The direction of the electric field is known as the direction of light's polarization vector. If we could see the rapid oscillations of the electric field inside a beam of light, we would find that its trajectory is very similar to one of the possible motions of the Foucault pendulum described above. The "state" of polarization is generally determined by the elliptical shape of the electric field and its angle, which can be changed by various optical devices such as polarizers. Shivaramakrishnan Pancharatnam studied the continuous changes in the polarization vector of light from its initial state to various states and back again. He found that the final oscillating state of the electric field was slightly different from the original polarization state, a phenomenon that could only be attributed to the specific polarization process. This phenomenon, which Pancharatnam discovered many years ago, is an example of geometric phases. A similar geometric phase can be observed for light propagating in a fibre optic cable when the direction of propagation is changed on a closed-loop.

The third example is from quantum physics. The geometric phase is also quite common in the quantum system because of the oscillating nature of the wave function. Consider a quantum system whose Hamiltonian $\boldsymbol{H}$ is assumed to depend on some control parameters (λ_1, λ_2...), as $\boldsymbol{H(\lambda)}$, and the parameter space is denoted as $\boldsymbol{M}$. Now suppose we adjust the control parameters very slowly on a path C in the parameter space. Suppose the system is initially in an eigenstate energy $|\psi(\lambda)\rangle = |u_n(\lambda)\rangle$ ($|u_n(\lambda)\rangle$ is the n^{th} eigen energy state), and assume that at each parameter point corresponding to path C, there is no crossover between corresponding energy levels. Then, if we adjust the parameters slow enough, the system will always stay in the same eigenstate $|\psi(\lambda(t))\rangle$. However, the wavefunction can differ by a phase factor, so the eigenstate instantaneous $|\psi(\lambda(t))\rangle$ can still differ a backlog of phase factors. Michael Berry from Bristol University found that in some physical cases, after deducting the kinetic phase, the wavefunction does not go back to initial states,

but accumulates an additional phase which is called the Berry phase.

The instantaneous energy eigenequation of the system is:

$$H(\lambda)|\ \psi(\lambda)\rangle = E(\lambda)|\ \psi(\lambda)\rangle \tag{4.2.1}$$

Where $E(\lambda) = E_n(\lambda)$ is the eigenenergy of the n^{th} energy eigenstate. According to the previous statement, as long as we adjust the parameters slowly enough, we can write the quantum state of the system as it evolves as follows:

$$|\ \Psi(t)\rangle = e^{iyt}\ \big|\ \psi\big(\lambda(t)\big)\big\rangle \tag{4.2.2}$$

In the formula, e^{iyt} is the undetermined phase factor mentioned in the previous paragraph. The time evolution state $|\ \Psi(t)\rangle$ generation into the time evolution of the Schrodinger equation $i\hbar\frac{\partial}{\partial t}|\ \Psi(t)\rangle = H(\lambda(t))|\ \Psi(t)\rangle$, we can get:

$$\left[-\hbar\dot{\gamma}\frac{\partial}{\partial t} + i\hbar\frac{\partial}{\partial t}\right]|\ \psi\big(\lambda(t)\big)\rangle = E\big(\lambda(t)\big)|\ \psi\big(\lambda(t)\big)\rangle \tag{4.2.3}$$

Using the bra $\big|\ \psi\big(\lambda(t)\big)\big\rangle$ to and the inner product of the equation, we can get:

$$\dot{\gamma} = \frac{E\big(\lambda(t)\big)}{\hbar} - i\left\langle\psi\big(\lambda(t)\big)\right|\frac{\partial}{\partial t}\left|\psi\big(\lambda(t)\big)\right\rangle \tag{4.2.4}$$

If we integrate this equation with respect to time, we get:

$$\gamma\big(t_f\big) - \gamma(t_i) = -\int_{t_i}^{t_f}\frac{E\big(\lambda(t)\big)dt}{\hbar} - i\int_C d\lambda_i\left\langle\psi\big(\lambda(t)\big)\right|\frac{\partial}{\partial\lambda_i}\left|\psi\big(\lambda(t)\big)\right\rangle \tag{4.2.5}$$

The first term of this final expression is the ordinary dynamic evolution phase, and the second term is called the geometric phase because it depends only on the geometric path *C* of the parameter space.

The appearance of geometric phase behaviour has injected new possibilities into the development of modern optical devices. In the case of Pancharatnam−Berry phase

modulation, since the azimuth varies continuously in space, this mapping from azimuth to phase allows for continuous phase changes and thus allows for more drastic phase changes without introducing discontinuities at the boundaries of 2π and 0 modes. This is very different from traditional liquid crystal phase modulators, which use changes in the polar angle (or inclination angle) to modulate the phase, resulting in a discontinuity at the 2π mode boundary.

Based on this feature, many new lenses, gratings, and deflectors have been developed and show better optical properties. Pancharatnam -- Berry Lenses demonstrate better beam selectivity and faster optical response times[88]. Pancharatnam-Berry deflectors have large deflection angles, and light-based on phase modulation affects real light. This modulation allows good input and output coupling for waveguide-based AR devices [89]. Compared with traditional Holographic Gratings, Pancharatnam−Berry based reflective polarization volume grating can provide a much higher exponential contrast. Therefore, it shows higher efficiency and a greater angle of acceptance. A major difference between reflective volume grating and holographic gratings is polarization selectivity. Because holographic gratings are essentially tilted layers made of different isotropic materials, they are independent of polarization. On the other hand, reflective polarization volume is a uniaxial crystal with an inclined helical axis, which allows only one circularly polarized light to be deflected, while the other polarization will pass through. This increases the overall transmission of applications [90].

Chapter 5 Experimental setup and materials:

5.1 Materials and optical components used in the experiments

name	Supplier	Properties	Function
Glass slide	Thorlabs: CG15KH	1.5H (170 μm) Thickness and ± 5 μm Tolerance	Gold plating substrate
Index matching gel	Thorlabs: G608N3	Refractive Index at 589.3 nm: 1.4646	Filling the gap between the prism and the glass-gold slide
gold	Pi-kem	99.99% purity	Source of gold plating
Silicon wafer	/	Atomic level straight edge	Shades of different metal thicknesses.
polarizer	Thorlabs: LPVISE100-A	Ø1" 400-700 nm	Linear Polarizer with N-BK7 Windows.
Adjustable lens	Thorlabs: MVL25M23	25 mm EFL, f/1.4, for 2/3" C-mount format cameras, with lock	Concentrate light onto cameras.

BK7 right angle Prism	Thorlabs: PS911	L=25mm	Holding gold-glass slide; generating SPP
Wollaston prism	Thorlabs: WP10	20° Beam Separation, 350 nm - 2.3 µm	Separating S and P polarized light into two different path ways
Fiber Beam Collimator	Thorlabs: C40FC-A	f = 40 mm, FC/PC, ARC: 400 - 650 nm	Generating 400-650nm collimating beam
Laser1	Thorlabs: S1FC637	Fabry-Perot Benchtop Laser Source, 637 nm, 8.0 mW,	Laser source
Laser2	NKT photonics: Superk compact supercontinuum laser.	450-2400 nm	Laser source
CCD camera	ToupTek: TP705200A	C-mount USB2.0 CCD Camera	Image catching
CMOS camera	Thorlabs: CS126MU	Kiralux 12.3 MP CMOS Compact Scientific Cameras USB3.0	Image catching

Sputter Coater	agar scientific	/	Making metal coating
Micro lens	Thorlabs: MVL12X3Z	12X Zoom Lens with 3 mm Fine Focus and Coaxial Illumination Port	Large magnification to help image fine features
PC	/	/	Data analysis camera software
30mm cage system	Thorlabs	/	Align the system
Si Free-Space Amplified Photodetectors	Thorlabs: PDA100A2	Si Switchable Gain Detector, 320 - 1100 nm, 11 MHz BW, 75.4 mm2	Detecting light intensity

Table 1 Materials and equipment using in this project.

5.2 Excitation of surface plasmon polaritons

First, I have investigated the excitation of surface plasmon polaritons using the Kretschmann configuration. Figure 19 shows the experimental setup consisting of a fibre-coupled 633 nm diode laser, fibre optic collimator, a high refractive index prism and a Si photodetector. Shining a laser beam on a flat metal surface cannot excite SPPs because of the momentum mismatch between the excitation light ($k_0 = \frac{2\pi}{\lambda}$) and SPP

($k_{spp} = n_{eff}k_0 > \ k_0$) To overcome the momentum mismatch we used a high glass prism with an index of refraction 1.5. When light enters into the prim the momentum increases to $n_p k_0$. This momentum increase enables us to match the momentum of SPP along the surface of the gold layer as $n_p k_0 \sin(\theta) = n_{eff}k_0$ where np=1.5 And n_{eff}=1.061.

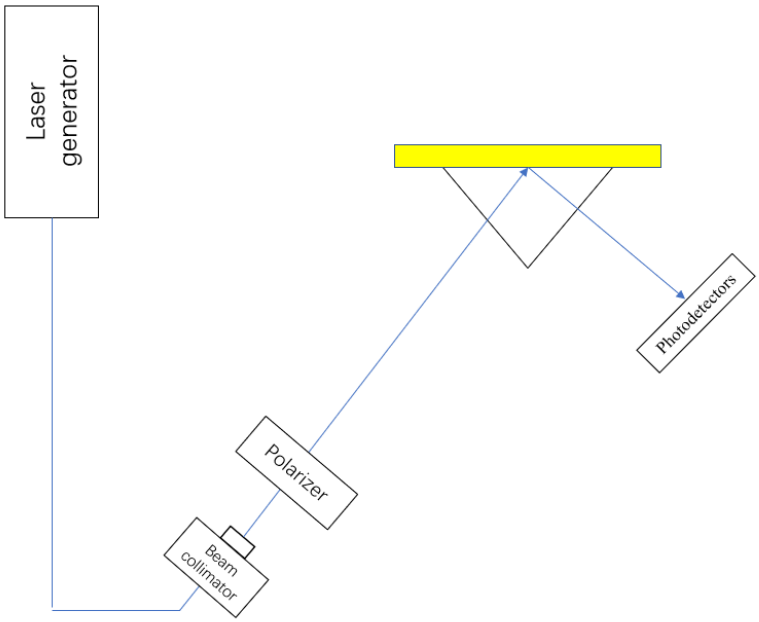

Figure 19 Experimental setup showing the excitation of surface plasmon polaritons with Kretschmann configuration. A thin layer of gold is coated on a glass slide and attached to a right-angle prism. The high refractive index prism enables overcoming the momentum mismatch between SPPs and excitation light.

I used a laser with a wavelength of 637nm as the excitation source. The output of the laser is made into a parallel beam by a fibre collimator. This beam of parallel light is polarized to P-polarized light after passing through a polymer polarizer. The P-polarized light then enters a right-angle prism. The light couples to the SPPs on the gold-air interface. By monitoring the intensity of the reflected light, we observe the excitation of SPPs. The intensity of the reflected light beam is detected by silicon

photodetectors.

The fibre collimator is precisely positioned by the tail fibre and the self-focusing lens. It can transform the transmitted light in the optical fibre into collimating light (parallel light) or coupling the external parallel (approximately parallel) light into the single-mode optical fibre. Its basic principle is that the lens can be used to transform a beam from a larger divergence angle (small waist) to a smaller divergence angle (large waist) so that it can be coupled into other optical devices with a lower loss.

The polarizer has the function of shielding and passing through the incident light, which can make the transverse light passing through or shielding. It is a composite material laminated by polarization film, inner protective film, pressure-sensitive adhesive layer and outer protective film. Polarized light is produced mainly due to the existence of its internal polarization film, which is a polymer material with a linear structure, so the beam will become polarized light after passing through the polarization film.

Photodetectors can transform light into an electrical signal in the optical communication system, which is mainly based on the photovoltaic effect of semiconductor materials. The so-called photovoltaic effect refers to the phenomenon that light causes a potential difference between different parts of a non-uniform semiconductor or a combination of a semiconductor and a metal. The basic working mechanism of photodetectors includes three processes: (1) photogenerated carriers are generated under light; (2) Current is formed by carrier diffusion or drift; (3) The photocurrent is amplified and converted into a voltage signal in the amplifier circuit. When the detector surface is irradiated by

light, if the material bandgap width is less than the energy of the incident light photon, i.e., Eg< hv, the valence band electron can transition to the conduction band to form a photocurrent if external field, or gradient of electron concentration exist.

I observed the excitation of SPPs by changing the incidence angle. At the resonance angle $n_p k_0 \sin(\theta) = n_{eff} k_0$ where the momentum of excitation matches the momentum of SPPs, the reflected intensity decreases due to the generation of SPPs. By changing the incident angle of the incoming light, we can have the characteristic reflection spectrum shown in Figure 20:

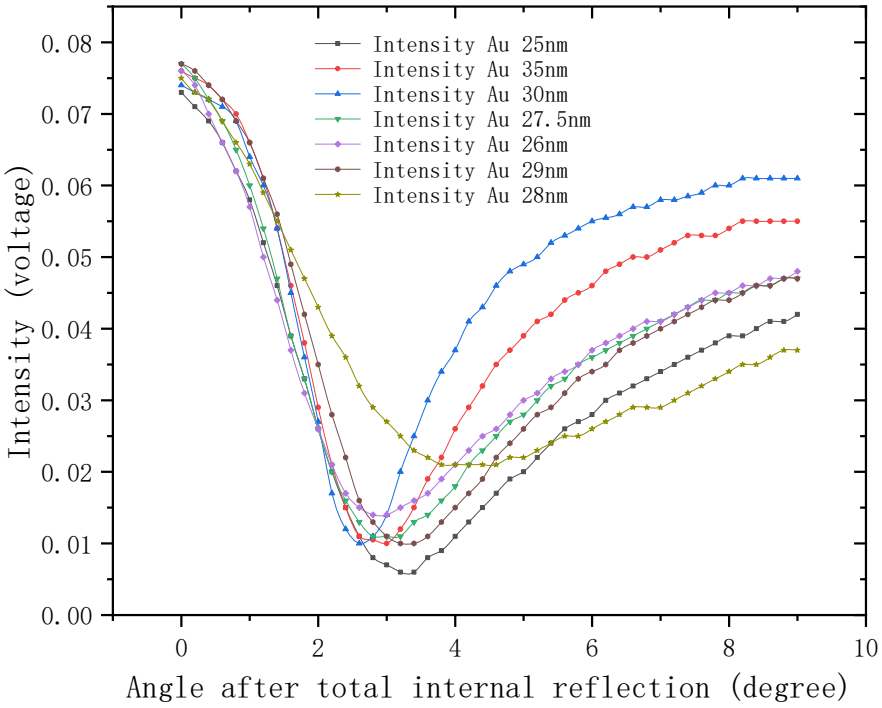

Figure 20 The variation of the reflected intensity as a function of incidence angle for different metal thicknesses. Here the resonance angle is 3 degrees more than the total internal reflection angle. Here metal thickness determines the efficiency of the SPP generation. I observe that 27.5 nm Au provides almost zero reflectivity at the resonance angle. This condition is known as the critical coupling condition which will play a very important role in the topological effects.

This experiment gave me a deeper understanding of surface plasmons and their excitation. The production of surface plasmons can happen when the energy of the light coincides with the excitation energy of the plasma on the metal. As it travels through the air, the momentum of light is less than the momentum of SPPs with the same energy. The prism is used to match the momentum of light and SPPs. Since only P-polarized light can excite SPPs, the change of incident angle adjusts the momentum value of the p-polarized wave along the metal surface. When the momentum is matched, a significant high optical absorption is observed in the reflected light.

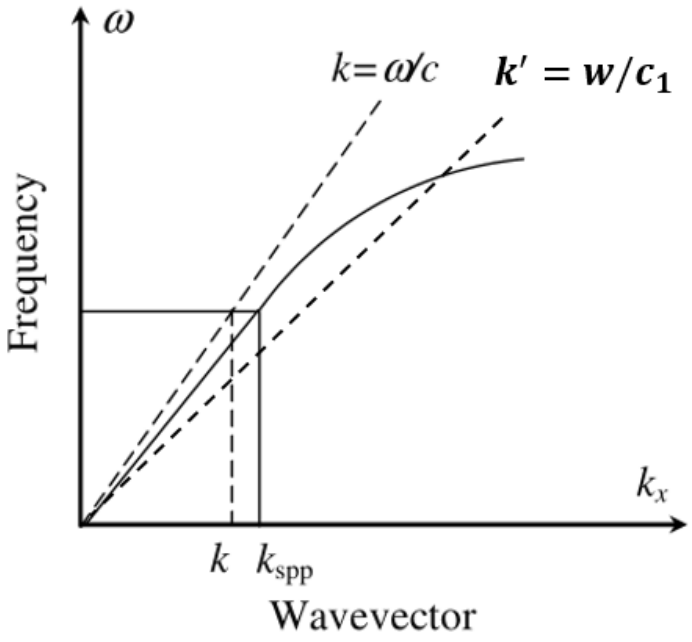

Figure 21 Dispersion curve of light and SPPs. This graph shows how the energy of light and SPP varies with the momentum. SPPs has higher momentum values than free propagating light due to their confined nature. For SPPs and light have the same energy, k_{SPP} is larger than k of photons. Because of this momentum mismatch, shining light on a flat metal does not generate plasmon polaritons. We need to overcome this momentum mismatch with a high refractive index prism which is known as the Kretschmann configuration.

The metal thickness determines the efficiency of the SPP generation. I first fabricated various metal films to find the critical metal thickness which provides the larges adsorption, which is known as the critical coupling condition where the reflected light becomes zero. This is an interesting condition because the phase of reflected light is not defined at this point. We realized that the critical thickness may bring a topological singular in surface plasmons.

To observe this topological singularity, I prepared a sample with two different thicknesses, one less than the critical thickness and the other more than the critical thickness. By imaging the reflected pattern, I observed an interesting feature: A distinct dark band appears at the junction of two different thicknesses. Through careful analysis, we preliminarily think that this phenomenon is produced by the change of reflection topology.

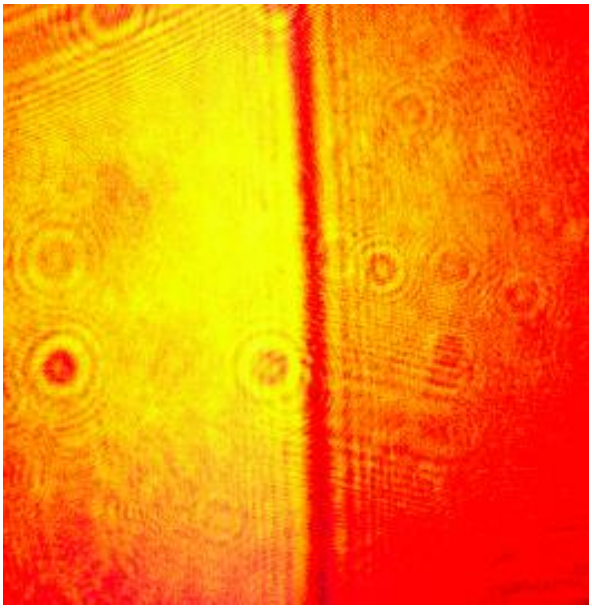

Figure 22 Image of the reflected light from the sample with two different metal thicknesses. one less than the critical thickness and the other more than the critical thickness. The dark line between at the boundary is due to a topological singularity where the phase of reflected light is not defined.

5.3 Experimental setup used for measurement of reflection phase

The main aim of this thesis is to measure the topological Berry phase of SPPs. Although the spectrum of reflected light can be measured with a simple spectrometer, measuring the phase of the reflected light is a challenging task. Here, the main technical issue is to separate the kinetic phase of light due to the propagation and the phase accumulation due to the geometrical or topological effects. Since the phase of light is a relative quantity, phase measurements require a reliable reference that does not change during the experiments. Only P-polarized light can generate SPPs, we decided to use S-polarized light as the reference. We have designed an optical setup resembling a spectroscopic ellipsometer which provides phase difference between S and P polarized light. The main working principle of this system is based on Fourier analysis of the interferogram generated by the S and P polarized light. Figure 23 shows the experimental setup and its schematic drawing. In this setup, we used a supercontinuum laser (SCL) as the light source. SCL generates a broadband (400-2600 nm) quasi-coherent light source which is collimated with and fibre collimator. The fibre collimator is placed on a rotary stage to control the incidence angle on the prism. We placed a broadband polarizer at 45^{o} angle to produce both S and P polarized light before the prism. Both S- P-polarized light propagate on the same optical path (i.e the same beam of light), the alignment of the interferometer is relatively easy. We placed the prism on another small rotary/tilt stage to compensate for the angle of the reflected light. After the reflection from the prism, the beam is split into S- P polarization using a Wollaston prism. WP consist of a two birefringent crystal that splits unpolarized incident light into

two orthogonally polarized outputs. After the WP, we used an imaging lens to merge these two orthogonally polarized outputs to a c-MOS camera. To form an interference pattern, we used a second polarizer (at 45º) after the imaging lens to convert the orthogonally polarized beams into 45º polarization. After the secondary polarizer, beams have the same polarization state therefore they can generate an interference pattern on the c-MOS camera.

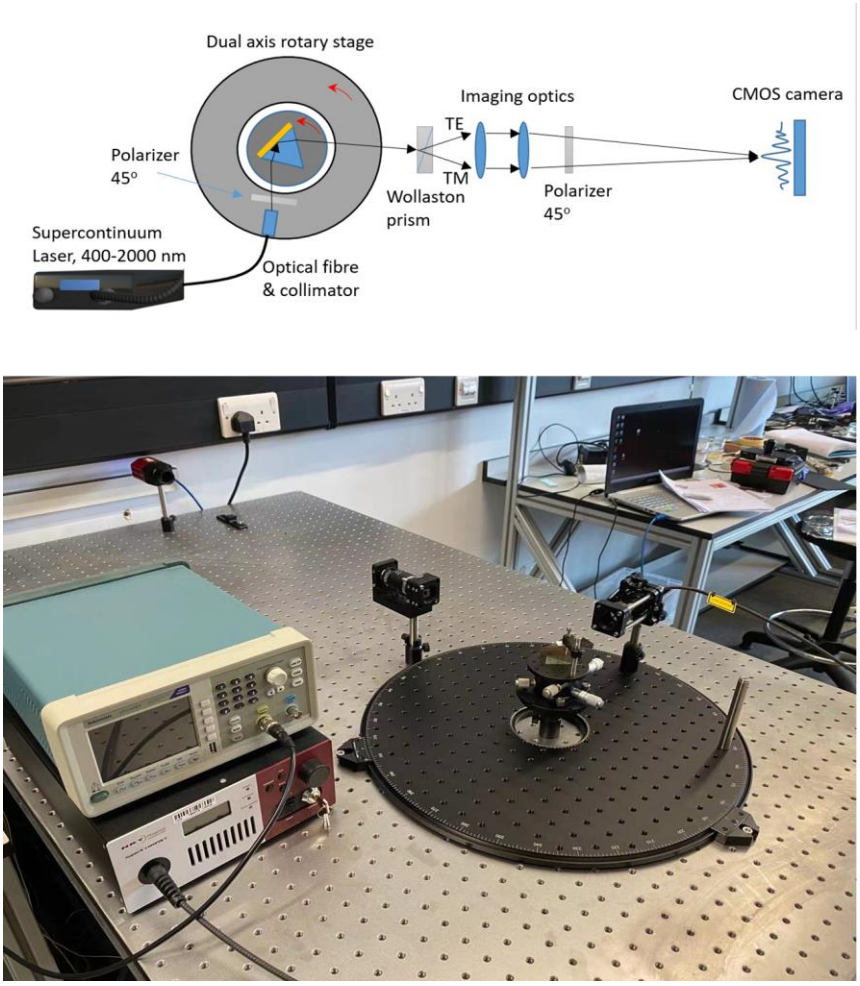

Figure 23 Schematics and photographs of the experimental setup used for the measurement of the reflection phase. The setup consists of a broadband supercontinuum laser, double-axis rotary stage, high refractive index prism, imaging lens and camera. We excite the SPPs using 45º polarized light. The reflected light is then split into s- and p-polarized light with a Wollaston prism. The interference of the beams on the camera generates an interferogram that includes both the intensity and phase of the reflected light.

5.4 Working principle of the Wollaston prism:

The Wollaston prism is an optical device that produces two beams of linearly polarized light that are separated from each other and have mutually perpendicular vibrational directions. It is composed of two right-angled prisms, and the material used is calcite. The optical axes of the two prisms are perpendicular to each other. When natural light is incident vertically on the surface of the Wollaston prism, the P-polarized light and S-polarized light propagate in the same direction without refraction, but at different speeds V, respectively. After they enter the second prism, the S-polarized light in the first prism becomes P-polarized light for the second prism because the optical axis of the second prism is perpendicular to that of the first prism, and the P-polarized light becomes S-polarized light for the second prism. Therefore, the S-polarized light in the first prism is refracted at the interface of the two prisms with the relative refractive index np/ns, while the P-polarized light in the first prism is refracted with the relative refractive index ns/np. Since calcite is a negative crystal (ns>np), the P-polarized light in the second prism propagates away from the normal at the intersection of the two calcites, and the S-polarized light in the second prism propagates close to the normal at the intersection of the two calcites. As a result, the two beams are separated in the second prism. Thus, the rightmost face is refracted again by the Wollaston prism and the two beams are polarized at a certain angle, and their vibrational directions are perpendicular to each other. When the angle at the top of the prism is not too large, the two refracted beams are separated almost symmetrically. The angle of separation of the

two beams is related to the material used in the Wollaston prism; if it is made of quartz, the angle of separation becomes much smaller.

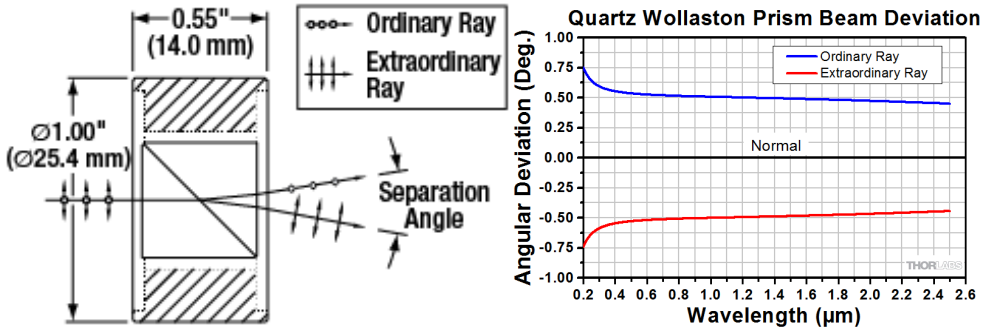

Figure 24 Schematic drawing of the Wollaston prism and the angular deviation as a function of wavelengths. (From Thorlabs Inc.)

5.5 Interferogram of broad-band light source:

To measure the phase spectrum of the reflected light, we created an interferogram using a broadband light source. The Fourier analysis of the interferogram provides the spectrum and phase difference ($\theta_s - \theta_p$). Figure 25 shows the optical path for the interferometer. Two orthogonally polarized outputs of the Wollaston prism (then converted to 45°) are merged on the camera with the imaging lens. We used a CMOS camera (Thorlabs CS126MU) with the number of active pixels 4096 (Horizontal) x 3000 (Vertical) and a total of about 12.3 million pixels. The pixel size is 3.45 µm x 3.45 µm. The imaging lens enhances the beam size which yields a position-dependent phase difference. The constant phase front of the beams is the plane perpendicular to the propagation direction. The zero-phase-difference (ZPD) position is at the centre of the

beam. Mowing away from the centre introduces an optical path difference (PD) $PD = x/\sin(\frac{\alpha}{2})$ where x is the position from the beam centre and α is the incidence angle of the beams. The period of the interference fringes can be calculated from a complete phase difference of pi, $\pi = kPD$ which makes $\Lambda = \lambda/2\sin\left(\frac{\alpha}{2}\right)$ which is equivalent to 20 pixels on the camera.

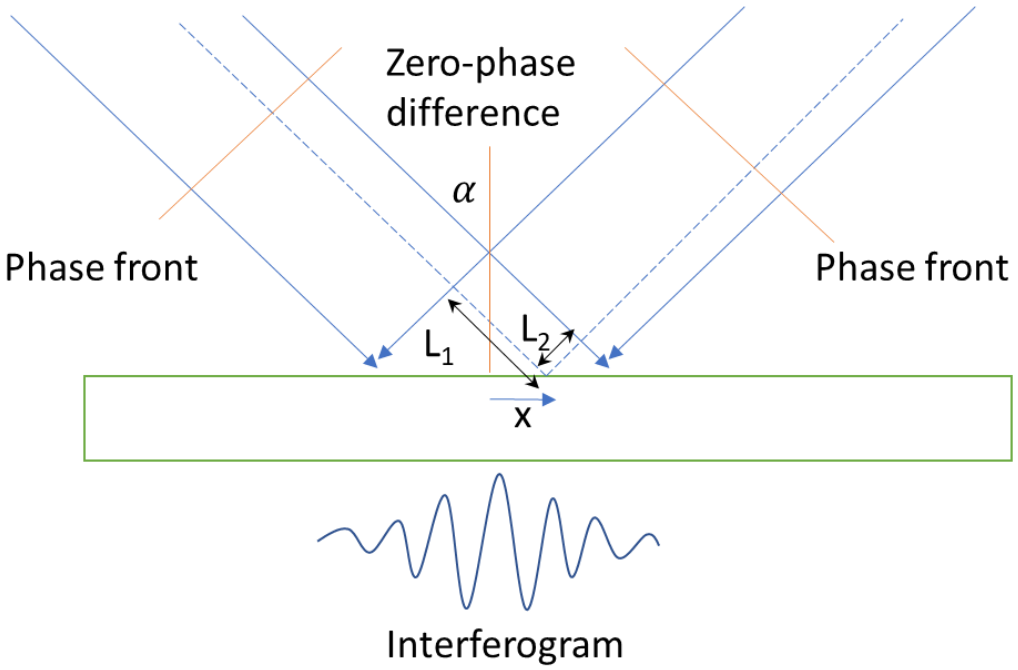

Figure 25 Schematic showing the optical path for the interferogram. Two orthogonally polarized outputs (then converted to 45°) are merged on the camera to generate an interference pattern on the camera. Because of the beam size of the outputs, there is position-dependent optical phase. The centre of the beam is the location of zero-phase difference.

Figure 26 shows a representative interferogram obtained from the camera image. The ZPD position is located at the centre of the image where all wavelengths interfere constructively generating the highest intensity. Mowing away from the ZPD yields a position-dependent oscillation depending on the spectrum and phase of the beams.

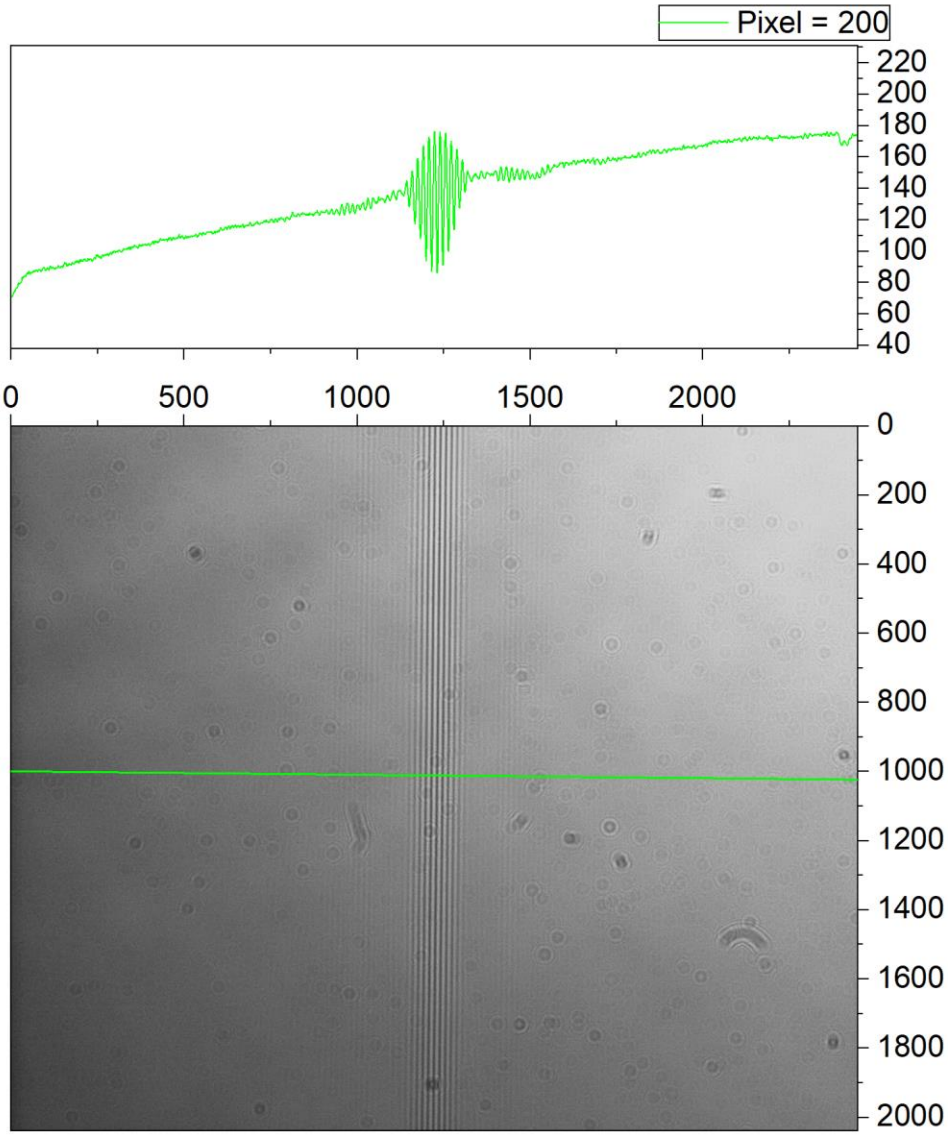

Figure 26 The recorded image and the graph shows the interferogram of the reflected light from the prism. Fourier analysis of the interferogram provides intensity and phase spectrum.

5.6 Fourier transform of the interferogram:

The interferogram contains information about the spectrum and the phase of the interfering beams. To obtain this information, we used Fourier analysis of the interferogram. This method has been extensively used for infrared spectrometers and magnetic resonance imaging. Here we implement Fourier transform algorithm to obtain the spectrum and phase between s and p polarized light.

When two beams merge and convert into one beam, the constructive beam can be written as:

$$E = E_1 e^{iwt} + E_2 e^{i(wt+\theta)} \tag{5.6.1}$$

Among them, θ is the phase difference between S polarized light and P polarized light. According to the results discussed previously.

$$\theta = k \cdot PD = \frac{kx}{sin\frac{\alpha}{2}} = \frac{2\pi x}{\lambda \cdot sin\frac{\alpha}{2}} \tag{5.6.2}$$

k is the wavenumber, which is $k = \frac{2\pi}{\lambda}$.

Due to the presence of the 45° polarizer, the intensity of the P-polarized light and S-polarized light are equal, thus: $E_1 = E_2 = E_0$, So we can have the intensity catching by the camera, which is:

$$I = |E \cdot E^*| = 2E_0^2(1 + cos\theta) = 2E_0^2(1 + \cos(k \cdot PD)) \tag{5.6.3}$$

then

$$I(PD) = I(k)(1 + cos\theta) = 2E_0^2(1 + \cos(k \cdot PD)) \tag{5.6.4}$$

where $\mathrm{I(k)} = 2\mathrm{E}_0^2$ is a constant that depends only upon k and $\mathrm{I(PD)}$ is the interferogram.

Thus, for all different wavevector, the intensity on the screen should be:

$$I(PD) = \int_0^\infty I(k)(1 + \cos(k \cdot PD))dPD \tag{5.6.5}$$

Written this equation into two parts: AC and DC

$$I_{DC}(PD) = \int_0^\infty I(k)dPD = \mathrm{I(k)} = 2\mathrm{E}_0^2 \tag{5.6.6}$$

which is a constant.

$$I_{AC}(PD) = \int_{0}^{\infty} I(k)\cos(k \cdot PD)\, dPD \tag{5.6.7}$$

Since COS function is an even function along x=0 axis, and cos(x) can be written as sin(ix), thus:

$$I_{AC}(PD) = \int_{-\infty}^{\infty} 2I(k)\cos(k \cdot PD)\, dPD$$

$$= \int_{-\infty}^{\infty} I(k)[cos(k \cdot PD) + isin(k \cdot PD)]dPD$$

$$= \int_{-\infty}^{\infty} I(k)e^{ikPD}dPD \tag{5.6.8}$$

Substitute (5.6.2) into (5.6.8), finally we have:

$$I(x) = 2\mathrm{E}_0^2 + \frac{1}{sin\frac{\alpha}{2}} \int_{-\infty}^{\infty} I(k)e^{ik\frac{x}{sin\frac{\alpha}{2}}}dx \tag{5.6.9}$$

From this equation, we proved the mathematical principles behind this Fourier transform visible spectrum. If any waveform can be transformed into a linear combination of constant, several sine and cosine functions, we can complete the conversion from the time domain to the frequency domain. This is the core idea of Fourier transformations: any continuous periodic signal can be combined by an appropriate set of sinusoidal curves.

Below is the spectrum and the phase information getting from Figure 26 based on this principle.

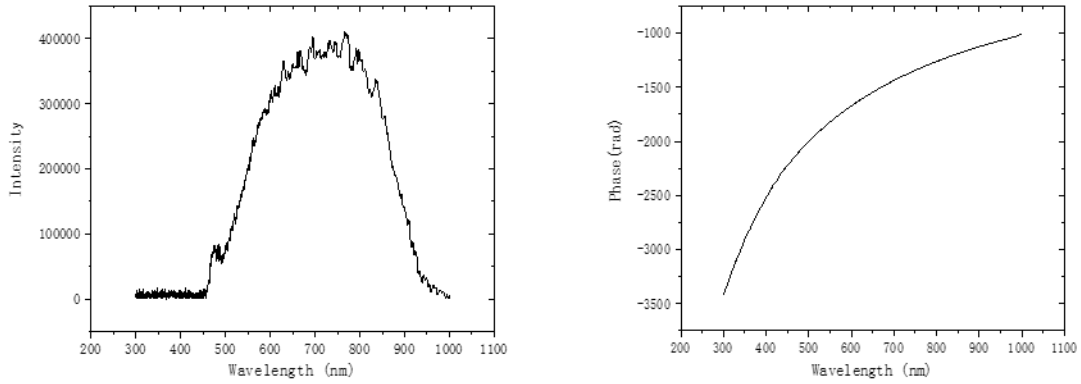

Figure 27 (a) Spectral and (b) phase changes of the beam obtained by Fourier transform visible interferogram.

5.7 Imaging camera:

We used an imaging camera to record the interferogram. There are currently two core imaging components of digital cameras: one is the widely used CCD (Charge Coupled Device) element; the other one is the CMOS (Complementary metal–oxide–semiconductor) device. Charge-coupled device image sensor CCD, which uses a high-sensitivity semiconductor material made of light into electric charge, through the analogue-to-digital converter chip into a digital signal, the digital signal after compression by the camera internal flash memory or built-in hard disk card to save, so you can easily transfer the data to the computer, and with the computer's processing means, according to the need and imagination to modify the image.

Complementary Metal-Oxide Semiconductor (CMOS) is the same semiconductor that records light changes in digital cameras as CCD. The current generated by these CCD and COMS complementary effects can be recorded and interpreted into images by the processing chip.

CCD and CMOS image sensor photoelectric conversion principle is the same, their main difference is that the signal readout process is different; because the CCD only one (or a few) output node unified readout, the consistency of its signal output is very good; and CMOS chip, each pixel has its signal amplifier, each charge-voltage conversion, the consistency of its signal output is poor. However, the CCD requires a wide signal bandwidth of the output amplifier to read out the whole image signal, while in the CMOS chip, the bandwidth of the amplifier in each image element is lower, which greatly reduces the power consumption of the chip, which is the main reason why the CMOS chip consumes less power than the CCD. Despite the reduced power consumption, but millions of amplifier inconsistency brings a higher fixed noise, which is the inherent disadvantage of CMOS relative to CCD.

5.8 Data acquisition and analysis software:

To make data acquisition and analysis easier, we use LabView to simplify the process of measuring and analyzing data.

① We use the LabView code provided by ThorLabs official website to obtain the data of the camera's real-time photos, that is, the image information into the LabView block diagram.

② This program execution block diagram shows the logical relationship between data measurement and processing. After the image is taken, the image data is converted into a matrix by the "Get Image Data" module, that is, the image is converted into the intensity of light on each pixel.

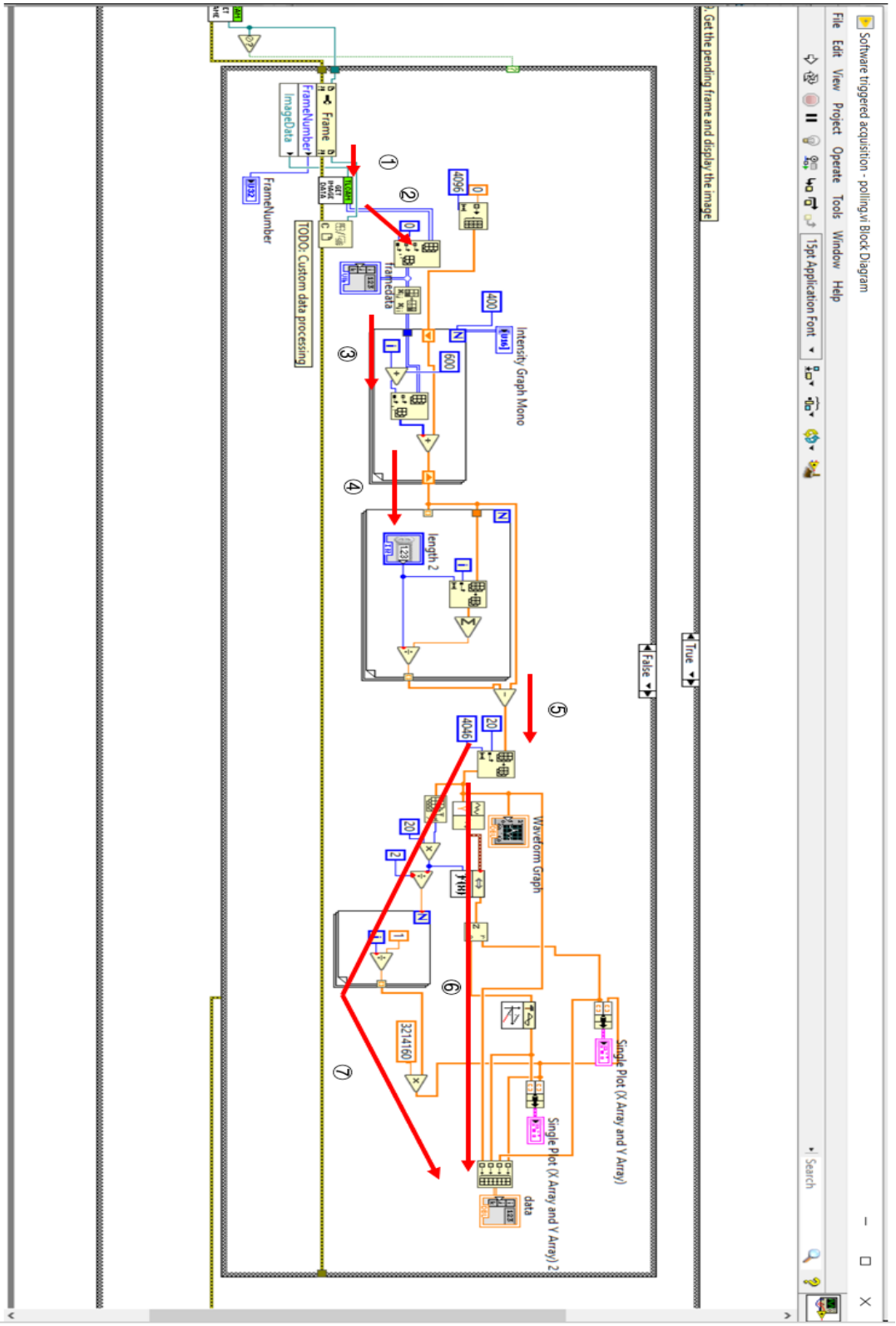

Figure 28 The LabView program logic block diagram of the interferometer to perform data acquisition and analysis.

③ In this step, the Image data matrix is first transposed to obtain the strength data of the image horizontal lines, and then input into a for loop statement to take multiple horizontal lines for analysis. The meaning of "400" is to take a total of 600 horizontal lines from the 400th pixel vertical and average them. The orange line is connected to the meaning of filling the rest of the data obtained by the average with zeros to form a matrix for the convenience of subsequent calculation.

④ The fourth step is to eliminate noise. As shown in Figure 26, the curve of intensity showed a linear increase, which was caused by noise and background. To reduce its influence, we subtracted the sum of a horizontal intensity from the obtained data and divided it by a constant correction curve, so as to obtain a noise-cancelling, flat interference pattern intensity curve.

⑤ The fifth step is to screen the data. Since the interference pattern is concentrated in the middle part of the whole image, in order to improve the operation efficiency of the program and save time, we choose the intensity of 20-4046 pixels in the horizontal direction and re-make it into a new matrix.

⑥ The sixth step is to Fourier transform the data to obtain spectral and phase information. First, the "Build waveform" module was used to enable LabView to identify and process the data, and then Fourier transform was performed on the data. The obtained data were spectrographs and phase changes, which were the key information of the experiment and the most important part of our requirements. When finished, it is imported into the output module.

⑦ This step is the method and logic of determining the wavelength of the spectrum." 3214160 "is the result of correcting the software results in reverse for a given wavelength range by using different filters.

This figure below is the front panel of LabView and a block diagram of its results. The processed data will be displayed here. It should be noted that since the CMOS camera

here is made of a silicon, the maximum wavelength that can be detected is 1100 nm. By the above method, we have built a new interferometer for the 300-1100 nm band and can change the angle of incidence for angular scanning.

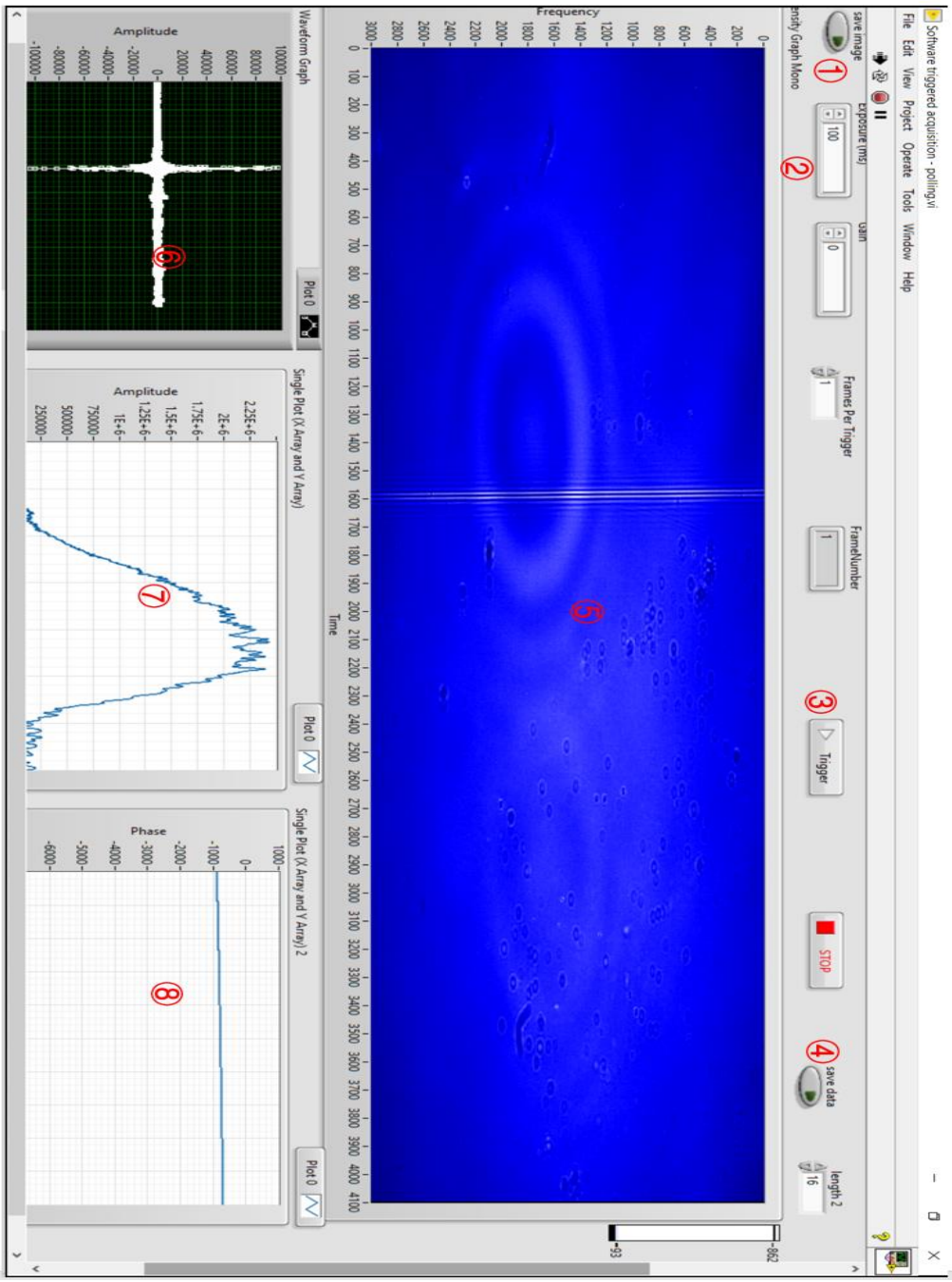

Figure 29 Block diagram of the Labview results of the interferometer. ① and ④ are image and data saving buttons, respectively. ②Exposure time setting box. ③ Single data acquisition and processing run button. ⑤ Display of the acquisition image. ⑥Waveform graph of the interference curve. ⑦Spectrum diagram of the measured light. ⑧Phase change of the measured light.

5.9 Sample preparation method:

We use index matching gel to connect BK7 prism and gold on glass slide together and the gold(99.99% Pi-Kem) coating is deposited on the surface of the glass by magnetron sputtering (agar scientific： High-Resolution Sputter Coater AGB7234).

Magnetron sputtering coating starts by placing the substrate or substrates to be deposited with thin films on the anode of the DC power supply of the magnetron sputtering system (high potential) and placing the original material of the thin film to be generated on the substrate as the sputtering target (to be bombarded by ions to be ionized) on the cathode of the magnetron sputtering system. Subsequently, the working chamber of the magnetron sputtering system is pumped to a certain air pressure under vacuum and certain air pressure of Argon (Ar) gas is passed to maintain the air pressure inside the chamber. Then the system is operated to energize the cathode and anode, and the voltage is gradually increased. After reaching a certain voltage, a glow discharge phenomenon is generated between the cathode and anode, and a large number of electrons and Ar ions are produced. Due to the electric field of the cathode and anode, the electron accelerates toward the anode, while the magnetic field near the cathode binds the range of motion of the electron (Lorentz force does not do work and does not affect the kinetic energy) and gathers near the cathode, which significantly increases the concentration of plasma near the target, so the electron does a compound motion of pendulum and spiral motion near the cathode due to Lorentz force and electric field force, and keeps hitting the Ar ions are positively charged, and the generated large amount of Ar ions are accelerated to the target of the cathode under the action of electric field, bombarding the target with Ar ions, which on the one hand leads to part of the target surface atoms gaining recoil energy and leaving the target surface to become sputtered atoms and finally deposited on the substrate surface; on the other hand leads to secondary electrons being emitted from the target surface and accelerated into the glow discharge plasma under the action of the cathode target sheath layer. The secondary electrons are accelerated into the glow discharge plasma region under the

action of the cathode target sheath. The secondary electrons entering the plasma region are bound by the magnetic field at the target surface and collide with the sputtering gas atoms to ionize them, so the secondary electrons are an important source of energy for the magnetron discharge to be self-sustaining.

Magnetron sputtering can be used to prepare a variety of materials such as metals, semiconductors, and insulators, and has the advantages of simple equipment, easy control, large coating area, and strong adhesion.

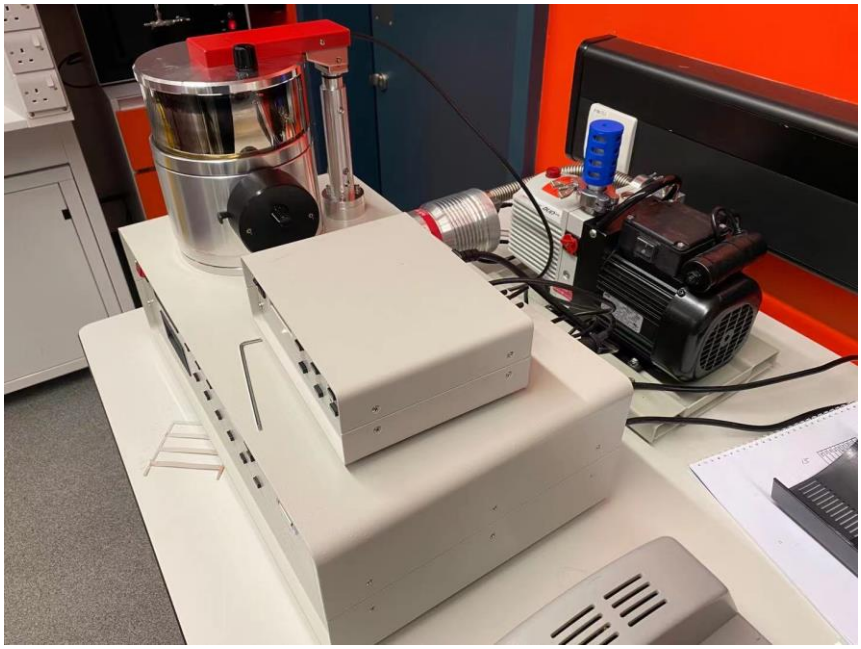

Figure 30 Desktop sputtering system used for the deposition of metal for surface plasmonic experiments.

To obtain a relatively sharp boundary between a thick and a thin metal coating, we used silicon wafers as the shadow mask of the thin metal coating during the production of the thick metal coating due to the unique atomic structure of silicon.

Chapter 6 Results and discussion:

In this chapter, I will discuss the experimental observation of the Berry phase for excitation of surface plasmon polaritons using the Kretschmann configuration shown in Figure 31a. We used a high refractive index prism to excite surface plasmon on a thin metal coated on a glass substrate. When the light goes into the prism and is reflected at the gold/glass interface, the free electrons in the gold layer are subjected to the action of an external electromagnetic field producing a collective forced vibration. SPP on the gold/air interface is excited by the evanescent electric field. The role of the prism is to overcome the momentum mismatch between SPP and light. The dispersion curve of SPPs is located outside the light cone and possesses a larger wave vector than the light with the same energy. Due to the strong optical absorption of the metal in the visible wavelengths, the propagation distance for the polaritons at the interface is usually only a few microns.

In our experiment, we predict that the metal thickness is a vital parameter that can shift the topology in the light reflection in this structure. The topological change can lead to drastic phase modulation. When there is topological change, that is the metal thickness is changed, there should be a strong change in the reflection. As shown in figure 31b, due to the topological theory, if you want to change the blue loop into the red one, you must cross the singularity point.

This singularity can provide us with a new method to control light and its phase.

In the Kretschmann configuration, the reflected light includes two components, (1) light directly reflected from the gold/glass interface, (2) light that outcouples from the SPPs. The second component is out of phase from the directly reflected light. The interference of these out of phase components forms two distinct topologies indicated the dominant component. By tuning the thickness of the metal layer, we can control the reflection topology.

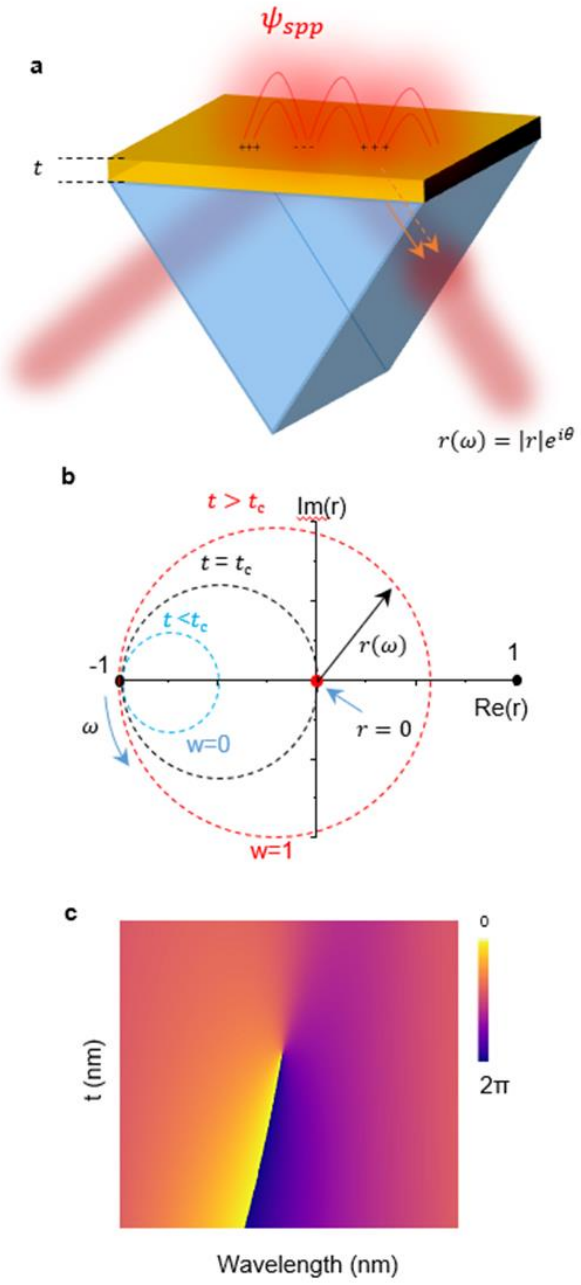

Figure 31 (a), Schematic representation of the Kretschmann configuration used for the observation of the Berry phase. The topology of the reflection is defined by the two-phase component coming from the direct reflection and outcoupling from the SPP. The thickness of the metal layer defines the ratio of the out of phase components and the resulting topology. (b), The complex representation of the Fresnel reflection coefficient forms a closed loop. The winding number of these loops defines the topology. (c), The map of the reflection phase is plotted as a function of the wavelength and thickness of the metal. The topological singularity with a charge of +1 is seen on the map.

The topology of the reflected light can be visualized using a complex reflectivity that

provides both amplitude and phase of the reflected light. Figure 31(b) shows the complex representation of the Fresnel reflection coefficient $r = |R|e^{i\theta}$ for three different metal thicknesses. As these three closed loops are placed in a coordinate system with Re r and Im r. The formation of the loop is plotted by sweeping the frequency of the excitation. The integer winding number of these loops defines the topology of the reflection. The reflection topology changes when the metal thickness is varies. Three different loops represent the reflection coefficients for three different metal thicknesses. Here the topological phase transition occurs at the critical metal thickness which generates zero reflectivity. Zero reflection is an indication of a phase singularity. When r=0, the phase of light is not defined. Winding this singularity point provides topologically different reflection which provides 2π Berry phase.

The metal thickness of the blue loop is less than the critical thickness, and there is no singularity in the blue loop, so its winding number is 0. The thickness of the black loop is exactly equal to the critical thickness. Thus, there is exactly a singularity point in its path, so its winding number is not defined for the critical metal thickness. The thickness of the red loop is larger than the critical thickness, there is a singularity inside the loop, which means its winding number is 1. Note that, all three loops pass through the point r=-1 indicating the direct reflectivity from a metal surface with a pi phase shift.

Figure 31(c) is the phase map of the complex reflection coefficient defined by two parameters, the wavelength and thickness of the metal. The results of the simulation show that there is a singularity with a topological charge of +1 in the parameter space. When the metal thickness is larger than the critical thickness, there is an additional phase accumulation of 2π. This additional phase accumulation is called the Berry phase. From a broader view, when the system goes back to initial conditions after mowing a closed loop, the system accumulates an additional phase depending on the topology of the loop, i.e., winding number.

a

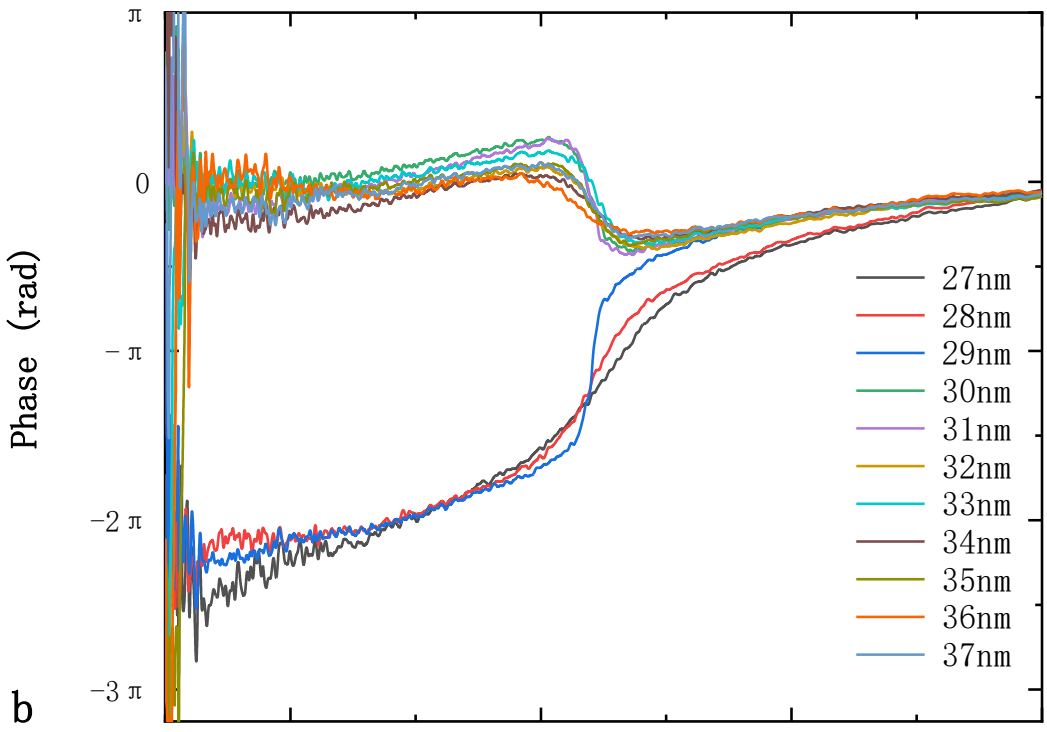
π
0
− π
−2 π
−3 π
Phase (rad)
500
600
700
800
Wavelength (nm)
27nm
28nm
29nm
30nm
31nm
32nm
33nm
34nm
35nm
36nm
37nm

b

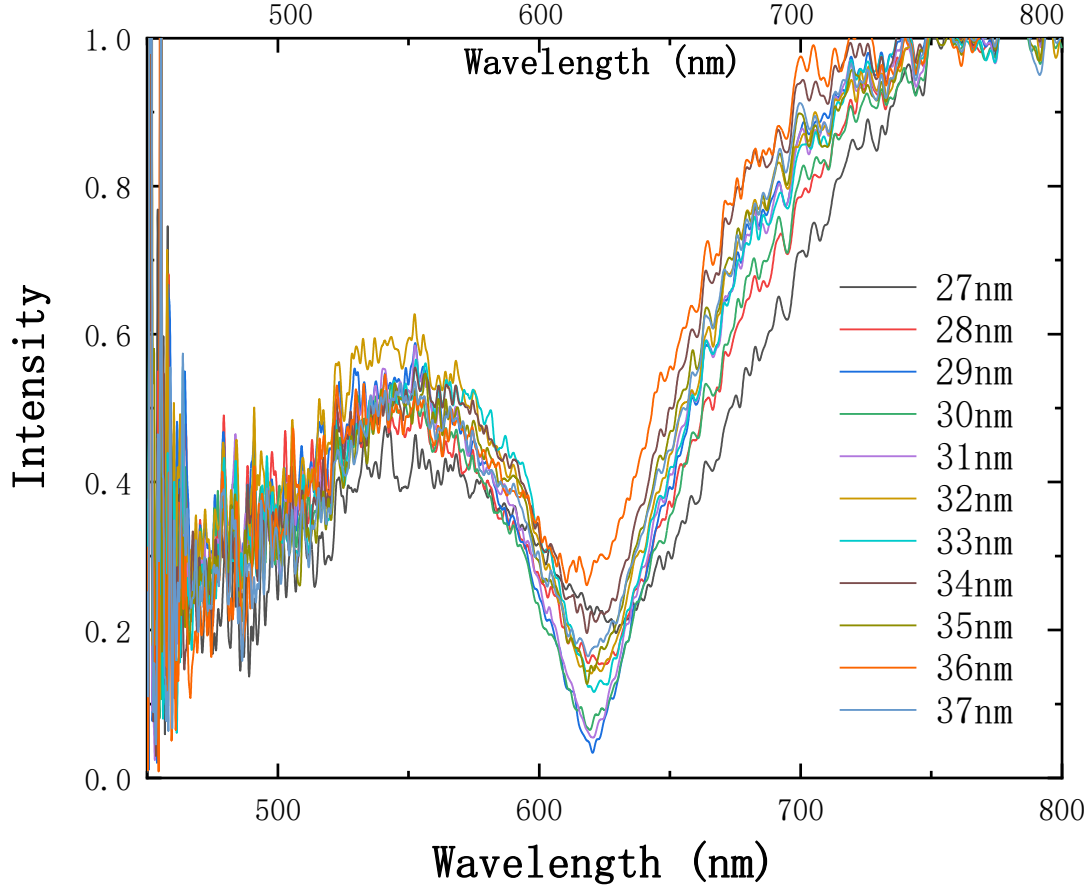
1.0
0.8
0.6
0.4
0.2
0.0
Intensity
500
600
700
800
Wavelength (nm)
27nm
28nm
29nm
30nm
31nm
32nm
33nm
34nm
35nm
36nm
37nm

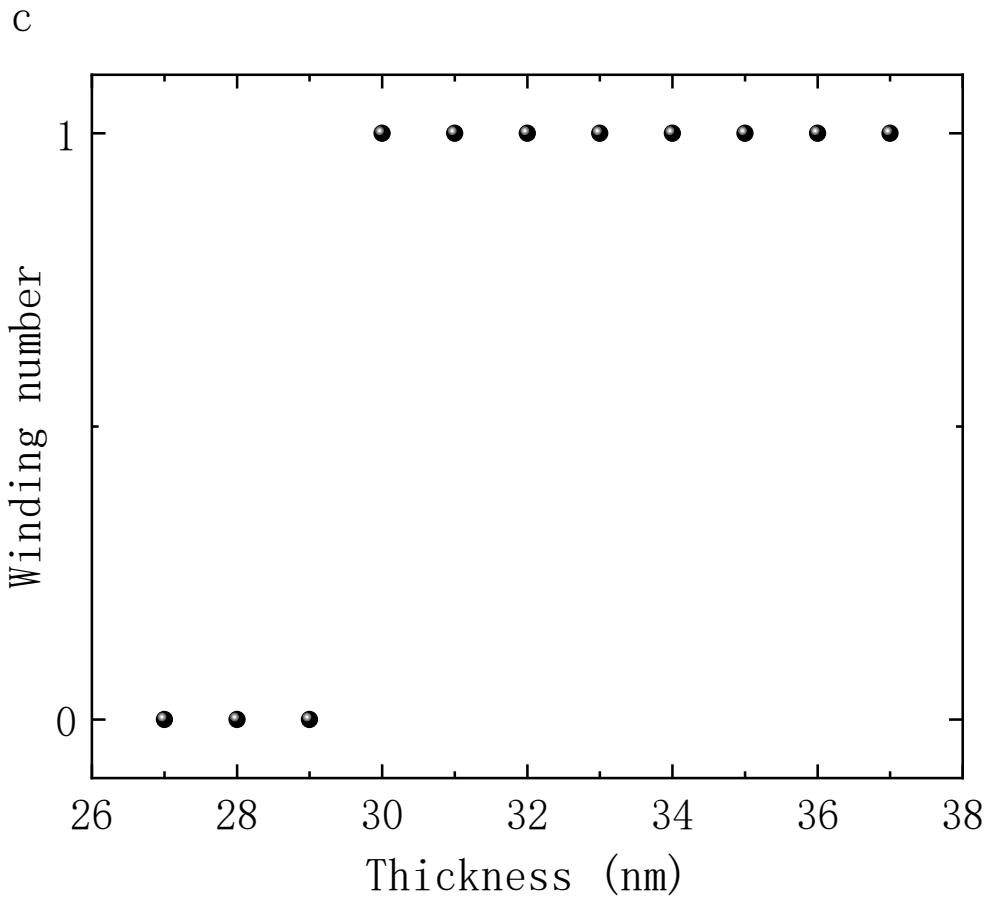

Figure 32: Experimental results showing the reflection phase and amplitude for different metal thickness for a spectral range from 450 to 800 nm. The critical metal thickness is between 29-30 nm. There is a clear difference in the phase behaviour for metal thickness larger less 29nm. There is an additional phase accumulation of 2π. c, shows the winding number of the reflection curves as a function of metal thickness. The topological phase transition happens around 29.5 nm.

Figure 32 shows the variation of intensity and phase change with the wavelength for different metal thicknesses. From Figure 32(a), we can see two different phase behaviours. For metal thickness >30nm, the curves show phase variation with the wavelength from 450nm to 800nm. After sweeping the wavelength from 450nm to 800 nm, the reflection phase goes back to the same value without any additional phase. However, for metal thickness, <30nm we observed a phase accumulation of 2π. There is a steep phase change around the resonance. The phase change is sharper around the

resonance for the critical thickness because the critical thickness can be treated as a singularity and the phase is not defined at this point.

In this figure, the resonance occurs at around 620 nm. As the gold thickness increases, the absorption at resonance increases with the metal thickness starting at 27 nm and reaches a maximum at 29 nm, reaching about 95% absorption. However, when the thickness changes to 30 nm, the absorption rate at resonance decreases compared with 29nm and with the increase of the metal layer thickness, the adsorption is lower and lower.

It is worth noting that a reference is needed for the phase measurements. We used the phase of the beam passing through a right-angle prism without a metal coating. This reference is subtracted from the measured results to obtain the final phase change diagram for different metal thickness layers. We also normalized the reflection intensity using the spectrum recorded from the bare prism.

Figure 32(c) represents the winding number for different gold metal thickness. For thickness of 27, 28 and 29nm, the winding number is 0; for thickness larger than 30nm, the winding number is 1 indicating different topological invariant for different thickness.

Figure 33 shows the domain colour map obtained from the experimental results. The horizontal axis indicates the metal thickness, and the vertical columns indicate the variation of wavelengths at the same thickness. There is a clear line in the upper left part of the diagram, showing a 2π phase shift starting at the singularity. This map indicates two different topological domains. Thick metal generates a trivial reflection with zero Berry phase. Thin metals <30nm, generate a nontrivial reflection with a 2π Berry phase. We believe that this is the first observation of the Berry phase for surface plasmons.

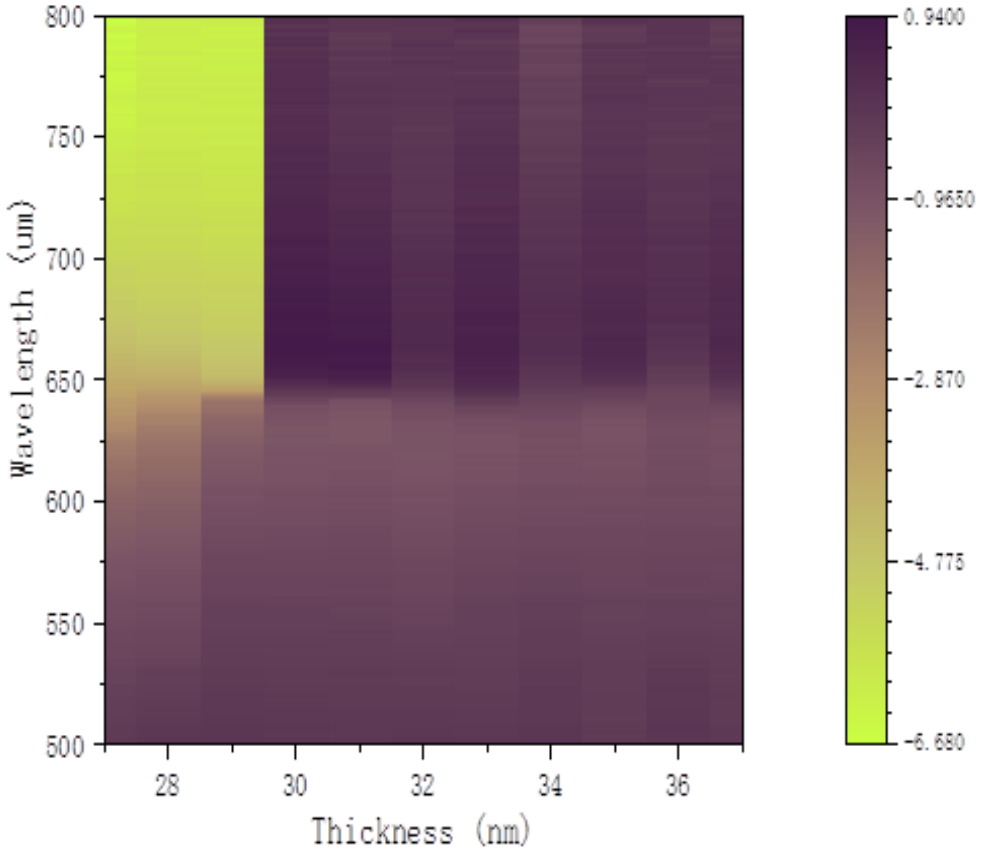

Figure 33 Experimentally obtained phase map of reflection plotted against thickness and wavelength. The phase singularity is around 620nm and 29 nm thick film.

Next, we would like to study the boundary between two regions with different reflection topologies. The hallmark of topological systems is the robust boundary modes between topologically distinct regions. For example, in condensed matter systems, the boundary between two topologically different semiconductors shows metallic behaviour because of the requirement of a zero bandgap at the boundary. Similarly in photonic systems, photonic crystal with a photonic bandgap shows waveguide modes at the boundary between two topologically different domains. The unifying concept of these topological boundary modes is the out of phase response of these domains at the boundary. In our system, we expect to see a boundary mode, a region with strong absorption, between

two regions with metal thickness less and higher than the critical thickness.

As discussed before, to verify this strange phenomenon caused by the change of metal thickness and to explore what exactly it is, we made an NK7 glass piece plated with different thicknesses of gold, as shown in (a), one is larger than the critical coupling thickness and the other is smaller. When we shine single-wavelength light on this junction area, we can get a black dark line as shown in Figure 34, and after measurement we find that the light intensity of this line is 0, indicating that this thickness junction region produces perfect 100% absorption.

To prove that this behaviour is coming from the topological change of the structure, we made use of the Fourier visible interferometer introduced in our previous experimental section. The light reflected through the thickness junction region was made into an interferogram pattern by such an experimental setup as shown in Figure 23. In this picture, there is a clear straight dark line in the middle, which is the boundary of different metal thicknesses. We can see that whether bright or dark lines, the upper and lower parts of the black boundary are not continuous, and there is always some offset that prevents these bright and dark lines from being straight, due to the phase transition. To determine the value of the phase transition more accurately, we took two different lines, the green and blue lines as shown in (c), on the interferogram pattern for each thickness and perform profile analysis on them.

(b) is the line profile of the two lines. we can see that there is a phase difference of π between the two lines, which is reflected in the plot, i.e., the peak of the blue line corresponds to the valley of the green line, while the peak of the green line corresponds to the valley of the blue line.

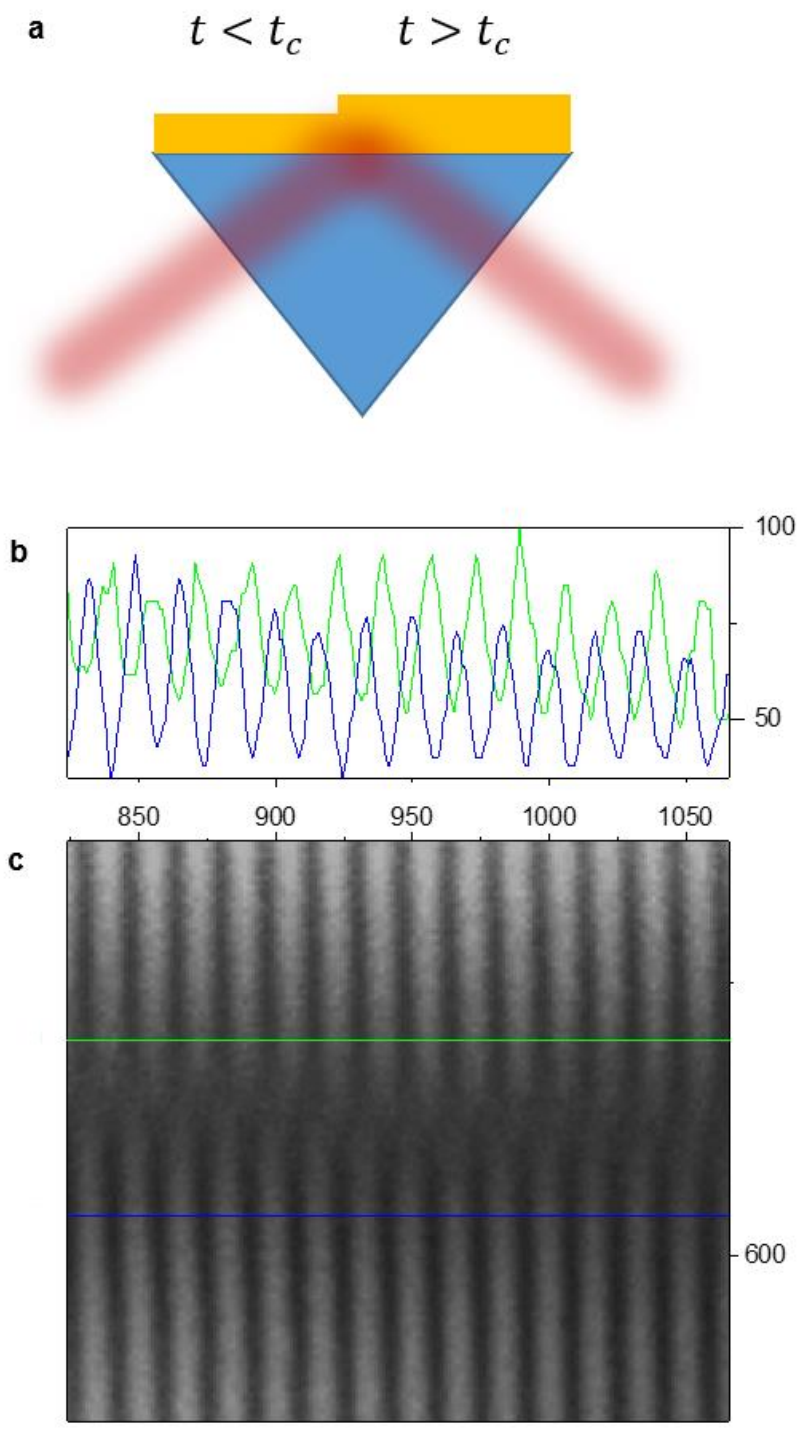

Figure 34. Schematic showing the excitation of SPPs on topologically different surfaces using a monochromatic light source which generates a uniform interference pattern. The interference pattern generated from these topologically different domains is out of phase.

Figure 35 shows us more about the perfect absorption of this topological change. In (a), we made four different thicknesses of gold plating, their thickness relationship is $t_1 < t_2 < t_3 < t_c < t_4$, using a single wavelength light source irradiated at the junction area of the four thicknesses and observe the reflected image. In the figure, we can find that only when the thickness of the two metals between the inclusion of critical thickness, there will be a clear dark band, and not t_c not in the two-thickness range of gold plating at the border, there are no obvious black stripes.

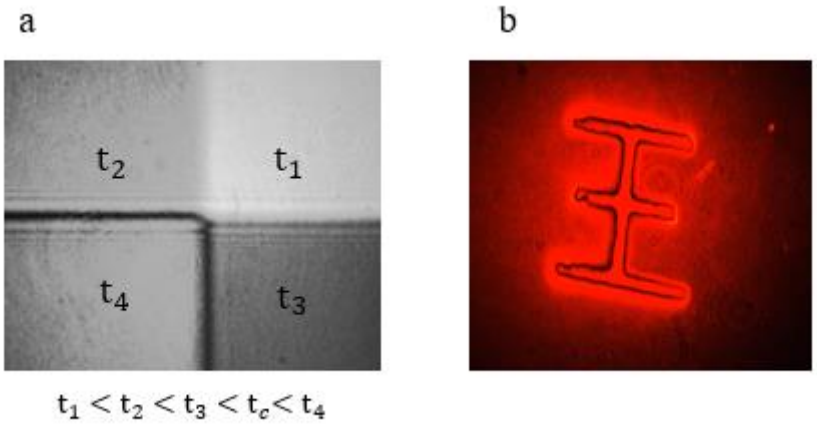

Figure 35 (a) An Image shows the reflection image from a surface with 4 different metal thicknesses. t_4 is topologically different from the rest, therefore there is a clear boundary mode around t4.(b) shows the reflection image from a pattern Chinese character "王" which demonstrate a boundary mode around the character.

In (b), a Chinese character "王" is shown. This symbol has a large plating thickness $t_s > t_c$ compared to the plating thickness of the substrate ($t < t_c$). From the image formed by the reflected beam, we can see that the Chinese character is wrapped in a distinct black stripe between the character and the substrate and that the nature of the stripe is not altered by the direction of the boundary, showing a uniform black colour. Not only that, some small features, such as imperfect boundaries when plated, can still be demonstrated, indicating the high resolution of this property. These above-mentioned features demonstrate the robustness of the characteristics brought about by this

topological change.

These results provide a piece of direct evidence for the topological character of the surface plasmon polaritons. The reflected light in the Kretschmann configuration includes two out of phase components, (1) directly reflected light from the metal surface and (2) the out coupled light from the surface plasmons. These two components are out of phase. The thickness of the metal determines the ratio of these components. When we reach the critical thickness, two components have the same amplitude therefore they interfere destructively generating zero reflection. By tuning the metal thickness we can change the topology of the reflectivity which tell which component is dominant. When the metal thickness is large, direct reflection is dominant resulting in a trivial topology. However, when the metal thickness is less than 30 nm, the outcoupled light is dominant resulting in a nontrivial topology with 2π Berry phase. The topology of the reflection appears on the complex reflectivity plane where the topological invariant is the winding number which can be express as:

$$w = \frac{1}{2\pi i}\oint \frac{dr}{r}$$

The winding number can take only integer values of 0 and 1. By tuning the metal thickness we can switch the topology of the reflection from the plasmonic surface. These topological features have consequences due to the bulk boundary correspondence principle. If we place two topologically different domains next to each other, at the boundary, we expect a localised boundary mode. We observe these localised modes in our case as perfect absorption lines around topologically different domains. These modes can be called non-Hermitian line modes which is a characteristic feature for lossy topological systems. These ideas can find different applications for optical devices however, they require electrical control of topological features. By electrically tuning the loss in the plasmonic system the topology can be switched by an electrical signal. This may enable an interesting device concept that uses topology to control the phase of light.

Chapter 7 Conclusion

As a summary, we present the observation of the Berry phase for the excitation of *surface plasmon polaritons*. Berry phase is a quantized geometrical phase that is determined by the topology of the system. In our experiments, the topological concept is related to the closed curves on complex reflectivity space. Our impedance analysis shows that the zero-reflectivity condition is a phase singularity on a complex reflectivity plane. The topology of the curves could be trivial or non-trivial depending on the encircling of the singularity point (zero-reflectivity r=0). We built an interferometric spectrometer to measure the phase and intensity of the reflected light in the visible spectrum. Using this experimental setup, we show that the topology of the reflection can be changed by tuning the thickness of the metal layer. The critical thickness provides the zero-reflectivity at the plasmonic resonance for p-polarized light. We studied the boundary between topologically different domains. We show that perfect P-polarized light absorption conditions appear at the boundary between topologically distinct regions. These topological patterns appear when the number of windings of the Fresnel reflection changes at the boundary. These perfect absorption lines are evidence for non- Hermitian edge modes that generate coherent localized light adsorption. The perfect adsorption coming from topologically protected robust property ensures that observing surface plasmon polaritons using a topological perspective will provide new insights and design tools that have potential applications in optical computing and optical artificial learning.

Being a materials science student, during this thesis, I have learned many new concepts in physics (such as wave impedance, topological physic) and I have gained a broad range of experiences in experimental optical techniques (including building optical setups, interferometers and data acquisition tools). It has been an interesting journey started from an idea of a mathematical concept of topology, building a new experimental setup and eventually observing a very abstract concept of Berry phase in

an experiment. I will prepare a scientific paper to report these observations. During my PhD study, I would like to extend this observation for other optical systems and want to build devices that exploit these unusual topological features of plasmons.

Reference:

[1]Bliokh, Konstantin Y., Daria Smirnova, and Franco Nori. Science 348.6242 (2015): 1448-1451.

[2] L Lu, JD Joannopoulos, M Soljačić Nature Photonics 8 (11), 821

[3] Klitzing K v, Dorda G, Pepper M 1980 Phys. Rev. Lett. 45 494

[4] Thouless D J, Kohmoto M, Nightingale M P, den Nijs M 1982 Phys. Rev. Lett. 49 405

[5] Kohmoto M 1985 Ann. Phys. 160 343

[6] Bernevig B. A., Hughes, T. L. & Zhang, S.-C. Science, 2006, 314: 1757

[7] Yablonovitch E. Phys. Rev. Lett., 1987, 58: 2059

[8] Haldane F D, Raghu S 2008 Phys. Rev. Lett. 100 013904

[9] Wang Z, Chong Y D, Joannopoulos J D, Soljacic M 2008 Phys. Rev. Lett. 100 013905

[10] Wang Z, Chong Y, Joannopoulos J D, Soljacic M 2009 Nature 461 772

[11] Skirlo S A, Lu L, Igarashi Y, Yan Q, Joannopoulos J, Soljacic M 2015 Phys. Rev. Lett. 115 253901

[12] Cheng X, Jouvaud C, Ni X, Mousavi S H, Genack A Z, Khanikaev A B 2016 Nat. Mater. 15 542

[13] Wu L H, Hu X 2015 Phys. Rev. Lett. 114 223901

[14] Nalitov A V, Malpuech G, Tercas H, Solnyshkov D D 2015 Phys. Rev. Lett. 114 026803

[15] Yang Y, Xu Y F, Xu T, Wang H X, Jiang J H, Hu X, Hang Z H 2018 Phys. Rev. Lett. 120 217401

[16] Khanikaev A B, Mousavi S H, Tse W K, Kargarian M, MacDonald A H, Shvets G 2013 Nat. Mater. 12 233

[17] Nathan F, Abanin D, Berg E, Lindner N H, Rudner M S 2019 Phys. Rev. B 99 195133

[18] Leykam D, Rechtsman M C, Chong Y D 2016 Phys. Rev.Lett. 117 013902

[19] Titum P, Lindner N H, Rechtsman M C, Refael G 2015 Phys. Rev. Lett. 114 056801

[20] Leykam D, Chong Y D 2016 Phys. Rev. Lett. 117 143901

[21] Mukherjee S, Spracklen A, Valiente M, Andersson E, Ohberg P, Goldman N, Thomson R R 2017 Nat. Commun. 813918

[22] Rechtsman M C, Zeuner J M, Plotnik Y, Lumer Y, Podolsky D, Dreisow F, Nolte S, Segev M, Szameit A 2013 Nature 496 196

[23] Fang K, Yu Z, Fan S 2012 Nat. Photonics 6 782

[24] Lumer Y, Plotnik Y, Rechtsman M C, Segev M 2013 Phys. Rev. Lett. 111 243905

[25] Mukherjee S, Chandrasekharan H K, Ohberg P, Goldman N, Thomson R R 2018 Nat. Commun. 9 4209

[26] Zhu B, Zhong H, Ke Y, Qin X, Sukhorukov A A, Kivshar Y S, Lee C 2018 Phys. Rev. A 98 013855

[27] Chen W J, Jiang S J, Chen X D, Zhu B, Zhou L, Dong J W, Chan C T 2014 Nat. Commun. 5 5782

[28] Chen Y, Chen H, Cai G 2018 Appl. Phys. Lett. 112 013504

[29] Hafezi M, Lukin M D, Taylor J M 2013 New J. Phys. 15 063001

[30] Harder G, Bartley T J, Lita A E, Nam S W, Gerrits T, Silberhorn C 2016 Phys. Rev. Lett. 116 143601

[31] Barik S, Karasahin A, Flower C, Cai T, Miyake H, DeGottardi W, Hafezi M, Waks E 2018 Science 359 666

[32] Lee T E 2016 Phys. Rev. Lett. 116 133903

[33] Kawabata K, Shiozaki K, Ueda M 2018 Phys. Rev. B 98 165148

[34] Kunst F K, Edvardsson E, Budich J C, Bergholtz E J 2018 Phys. Rev. Lett. 121 026808

[35] Wang H F, Gupta S K, Zhu X Y, Lu M H, Liu X P, Chen Y F 2018 Phys. Rev. B 98 214101

[36] Qi B, Zhang L, Ge L 2018 Phys. Rev. Lett. 120 093901

[37] Yao S, Song F, Wang Z 2018 Phys. Rev. Lett. 121 136802

[38] Feng L, El-Ganainy R, Ge L 2017 Nat. Photonics 11 752

[39] Midya B, Zhao H, Feng L 2018 Nat. Commun. 9 2674

[40] El-Ganainy R, Makris K G, Khajavikhan M, Musslimani Z H, Rotter S, Christodoulides D N 2018 Nat. Phys. 14 11

[41] Zeuner J M, Rechtsman M C, Plotnik Y, Lumer Y, Nolte S, Rudner M S, Segev M, Szameit A 2015 Phys. Rev. Lett. 115 040402

[42] Gupta S K, Zou Y, Zhu X Y, Lu M H, Zhang L, Liu X P, Chen Y F 2018 arXiv preprint arXiv: 1803.00794

[43] Regensburger A, Bersch C, Miri M A, Onishchukov G,Christodoulides D N, Peschel U 2012 Nature 488 167

[44] Bender C M, Boettcher S 1998 Phys. Rev. Lett. 80 5243

[45] Shen H, Zhen B, Fu L 2018 Phys. Rev. Lett. 120 146402

[46] Lieu S 2018 Phys. Rev. B 97 045106

[47] Malzard S, Poli C, Schomerus H 2015 Phys. Rev. Lett. 115 200402

[48] Soljačić M, Joannopoulos J D 2004 Nat. Mater. 3 211

[49] Dobrykh D A, Yulin A V, Slobozhanyuk A P, Poddubny A N, Kivshar Y S 2018 Phys. Rev. Lett. 121 163901

[50] Haddad L H, Weaver C M, Carr L D 2015 New J. Phys. 17 063033

[51] Soljačić M, Luo C, Joannopoulos J D, Fan S 2003 Opt. Lett.28 637

[52] Berger V 1998 Phys. Rev. Lett. 81 4136

[53] Adair R, Chase L L, Payne S A 1989 Phys. Rev. B 39 3337

[54] Fleischer J W, Segev M, Efremidis N K, Christodoulides D N 2003 Nature 422 147

[55] Zhou X, Wang Y, Leykam D, Chong Y D 2017 New J. Phys.19 095002

[56] Rajesh C, Georgios T 2019 arXiv: 1904.09466 v1

[57] Hadad Y, Khanikaev A B, Alù A 2016 Phys. Rev. B 93 155112

[58] Mingaleev S F, Kivshar Y S 2001 Phys. Rev. Lett. 86 5474

[59] Chen X D, Deng W M, Shi F L, Zhao F L, Chen M, Dong J W 2018 arXiv: 1812.08326

[60] Hu H, Huang B, Zhao E, Liu W V 2019 arXiv:1905.03727 v1

[61] Ezawa M 2018 Phys. Rev. B 98 201402

[62] Schindler F, Cook A M, Vergniory M G, Wang Z, Parkin S S, Bernevig B A, Neupert T 2018 Sci. Adv. 4 eaat0346

[63] Ezawa M 2018 Phys. Rev. Lett. 120 026801

[64] Khalaf E 2018 Phys. Rev. B 97 205136

[65] van Miert G, Ortix C 2018 Phys. Rev. B 98 081110

[66] Călugăru D, Juričić V, Roy B 2019 Phys. Rev. B 99 041301

[67] Kunst F K, van Miert G, Bergholtz E J 2018 Phys. Rev. B 97 241405

[68] Ezawa M 2018 Phys. Rev. B 97 155305[71]

[69] Ezawa M 2018 Phys. Rev. B 98 045125[72]

[70] Yasutomo O, Feng L, Ryota K, Katsuyuki W, Katsunori W, Yasuhiko A, Satoshi I 2018 arXiv: 1812.10171

[71] Peterson C W, Benalcazar W A, Hughes T L, Bahl G 2018 Nature 555 346

[72] Xie B Y, Wang H F, Wang H X, Zhu X Y, Jiang J H, Lu M H, Chen Y F 2018 Phys. Rev. B 98 205147

[73] Xie B Y, Su G X, Wang H F, Su H, Shen X P, Zhan P, Lu M H, Wang Z L, Chen Y F 2019 Phys. Rev. Lett. 122 233903

[74] Su W P, Schrieffer J R, Heeger A J 1979 Phys. Rev. Lett. 42 1698

[75] Asbóth JK, Oroszlány L, Pályi A. A short course on topological insulators, lecture notes in physics, Vol. 919. Cham, Switzerland, Springer International Publishing, 2016.

[76] St-Jean P, Goblot V, Galopin E, Lemaître A, Ozawa T, Le Gratiet L, Sagnes I, Bloch J, Amo A 2017

Nat. Photonics 11 651

[77] Parto M, Wittek S, Hodaei H, Harari G, Bandres M A, Ren J, Rechtsman M C, Segev M, Christodoulides D N, Khajavikhan M 2018 Phys. Rev. Lett. 120 113901

[78] He C, Sun X C, Liu X P, Lu M H, Chen Y, Feng L, Chen Y F 2016 Proc. Natl. Acad. Sci. USA 113 4924

[79] Hafezi, M., Demler, E., Lukin, M. *et al.*. *Nature Phys* **7,** 907–912 (2011).

[80] Hafezi, M., Mittal, S., Fan, J. et al. Nature Photon 7, 1001–1005 (2013).

[81] Rechtsman, M., Zeuner, J., Tünnermann, A. et al. Nature Photon 7, 153–158 (2013)

[82] Rechtsman, M., Plotnik, Y., Zeuner, J., Song, D., Chen, Z., Szameit, A. and Segev, M., 2013. Physical Review Letters, 111(10).

[83] Jerrard H. Journal of The Optical Society of America,1948, 38(1): 35-59.

[84] Zhao, Qiao, et al. Science 6458.365(2019):1163-1166.

[85] Maczewsky, L. et al..Science, 370(6517) (2020), .701-704.

[86] Wang, Y., Xie, BY., Lu, YH. et al. Light Sci Appl 10, 173 (2021).

[87] M. V. Berry.Proc. R. Soc. Lond. A 392 (1802): 45–57. 1984.

[88] J H Hannay 1985 *J. Phys. A: Math. Gen.* **18** 221

[89] Lee, Y. et al (2017) Optical Data Processing and Storage, Vol. 3 (Issue 1), pp. 79-88.

[90] K. Gao. et al. Opt. Express 25(6), 6283-6293 (2017).

[91] Phyx.readthedocs.io. 2021. Lecture 1 : 1-d SSH model — Physics 0.1 documentation. [online] Available at: <https://phyx.readthedocs.io/en/latest/TI/Lecture%20notes/1.html> [Accessed 17 September 2021].

[92] Rudner, M., Lindner, N., Berg, E. and Levin, M., 2013. Physical Review X, 3(3).

[93] Hatsugai, Y., 1993. Physical Review Letters, 71(22), pp.3697-3700.